JOURNAL OF PETROLOGY | VOLUME 00 | NUMBER 0 | PAGES 1–28 | 2008 | doi:10.1093/petrology/egn014
Journal of Petrology Advance Access published April 10, 2008

Origin of Pyroxenite–Peridotite Veined Mantle by Refertilization Reactions: Evidence from the Ronda Peridotite (Southern Spain)

JEAN-LOUIS BODINIER[1], CARLOS J. GARRIDO[2]*, INGRID CHANEFO[1], OLIVIER BRUGUIER[1] AND FERNANDO GERVILLA[2]

[1]GÉOSCIENCES MONTPELLIER, CNRS-UNIVERSITÉ DE MONTPELLIER II, CC 60, PLACE E. BATAILLON, 34095 MONTPELLIER, FRANCE

[2]INSTITUTO ANDALUZ DE CIENCIAS DE LA TIERRA (IACT), CSIC & UNIVERSIDAD DE GRANADA, FACULTAD DE CIENCIAS, 18002 GRANADA, SPAIN

RECEIVED FEBRUARY 10, 2007; ACCEPTED FEBRUARY 19, 2008

The Ronda orogenic peridotite (southern Spain) contains a variety of pyroxene-rich rocks ranging from high-pressure garnet granulites and pyroxenites to low-pressure plagioclase–spinel websterites. The 'asthenospherized' part of the Ronda peridotite contains abundant layered websterites ('group C' pyroxenites), without significant deformation, that occur as swarms of layers showing gradual modal transitions towards their host peridotites. Previous studies have suggested that these layered pyroxenites formed by the replacement of refractory spinel peridotites. Here, we present a major- and trace-element, and numerical modelling study of a layered outcrop of group C pyroxenite near the locality of Tolox aimed at constraining the origin of these pyroxenites after host peridotites by pervasive pyroxene-producing, refertilization melt–rock reactions. Mg-number [= Mg/(Mg + Fe) cationic ratio] numerical modelling shows that decreasing Mg-number with increasing pyroxene proportion, characteristic of Ronda group C pyroxenites, can be accounted for by a melt-consuming reaction resulting in the formation of mildly evolved, relatively low Mg-number melts (~0·65) provided that the melt fraction during reaction and the time-integrated melt/rock ratio are high enough (>0·1 and >1, respectively) to balance Mg–Fe buffering by peridotite minerals. This implies strong melt focusing caused by melt channelling in high-porosity domains resulting from compaction processes in a partial melted lithospheric domain below a solidus isotherm represented by the Ronda peridotite recrystallization front. The chondrite-normalized rare earth element (REE) patterns of group C whole-rocks and clinopyroxenes are convex-upward. Numerical modeling of REE variations in clinopyroxene produced by a pyroxene-forming, melt-consuming reaction results in curved trajectories in the $(Ce/Nd)_N$ vs $(Sm/Yb)_N$ diagram (where N indicates chondrite normalized). Based on $(Ce/Nd)_N$ values, two transient, enriched domains between the light REE (LREE)-depleted composition of the initial peridotite and that of the infiltrated melt may be distinguished in the reaction column: (1) a lower domain characterized by convex-upward REE patterns similar to those observed in Ronda group C pyroxenite–peridotite; (2) an upper domain characterized by melts with strongly LREE-enriched compositions. The latter are probably volatile-rich, small-volume melt fractions residual after the refertilization reactions that generated group C pyroxenites, which migrated throughout the massif—including the unmelted lithospheric spinel-tectonite domain. The Ronda mantle domains affected by pyroxenite- and dunite- or harzburgite-forming reactions (the 'layered granular' subdomain and 'plagioclase-tectonite' domain) are on average more fertile than the residual, 'coarse granular' subdomain at the recrystallization front. This indicates that refertilization traces the moving boundaries of receding cooling of a thinned and partially melted subcontinental lithosphere. This refertilization process may be widespread during transient thinning and melting of depleted subcontinental lithospheric mantle above upwelling asthenospheric mantle.

KEY WORDS: *subcontinental mantle; refertilization; pyroxenite; peridotite; websterite; melt–rock reaction; plagioclase; trace elements*

*Corresponding author. Telephone: +34 958 240 473. Fax: +34 958 243 368. E-mail: carlosg@ugr.es

INTRODUCTION

Many studies have invoked small (less than kilometer) scale heterogeneity of the Earth's mantle to provide sources for chemically and/or isotopically heterogeneous oceanic basalts (Hofmann & White, 1982; Allègre & Turcotte, 1986; Prinzhofer *et al.*, 1989; Hauri, 1996; Hirschmann & Stolper, 1996; Sobolev *et al.*, 2005; Herzberg, 2006). Preferential melting of pyroxenite or eclogite layers or veins would explain isotopic variations correlated with melting degree in oceanic basalts, and might also account for isotopic discrepancies between mid-ocean ridge basalt (MORB) and abyssal residual peridotites (Salters & Dick, 2002). The information conveyed by orogenic peridotite massifs is that mantle rocks may include a substantial amount of pyroxenitic lithologies, in the form of layers, veins and dykes (Bodinier & Godard, 2003, and references therein). Studies of pyroxenites in orogenic massifs may provide valuable information on the scale, distribution and extent of geochemical heterogeneities in the convective mantle. The origin of pyroxenitic and mafic lithologies in orogenic peridotites is controversial, particularly whether they are convective or lithospheric mantle features. The hypothesis that predominates for the origin of orogenic pyroxenite layers is that they are crystal segregates from mantle melts in magma conduits emplaced in the subcontinental lithospheric mantle and therefore they are not straightforward evidence for a veined convective mantle origin. Evidence for an igneous segregate origin is based on field, textural, and trace-element arguments such as cross-cutting relationships, igneous textures and heavy rare earth element (HREE) fractionation indicative of garnet fractionation (Shervais, 1979; Wilshire *et al.*, 1980; Bodinier *et al.*, 1987*a*, 1987*b*; Takazawa *et al.*, 1996; Garrido & Bodinier, 1999).

On the basis of the isotopic differences between pyroxenites and their host peridotites, and the existence of garnet pyroxenites with positive Eu anomalies, some orogenic pyroxenites have been interpreted as remnants of subducted oceanic crust stretched and thinned in the convective mantle (the 'marble cake' model of Allègre & Turcotte, 1986; see also Polvé & Allègre, 1980; Hamelin & Allègre, 1988; Kornprobst *et al.*, 1990; Pearson *et al.*, 1993; Blichert-Toft *et al.*, 1999; Morishita & Arai, 2001; Morishita *et al.*, 2001). This hypothesis is further supported by the detailed isotopic characterization (Nd–Sr–Pb–Hf–Os–S) of the ultrahigh-pressure (corundum- and diamond pseudomorph-bearing) garnet pyroxenites from Beni Bousera and Ronda (Pearson *et al.*, 1989, 1993; Davies *et al.*, 1993; Pearson & Nowell, 2004), which indicates a derivation from hydrothermally altered oceanic crust and hemi-pelagic sediments. However, all these researchers proposed that pyroxenites are segregates in vein conduits crystallized from partial melts of altered subducted oceanic crust. A similar origin has been proposed for pyroxenites in Lower Austria garnet peridotites (Becker, 1996; Becker *et al.*, 2004). All these pyroxenites are strongly deformed and underwent a high-pressure metamorphic evolution, associated with—or followed by—partial melting and/or high-temperature metasomatism (Loubet & Allègre, 1982; Pearson *et al.*, 1993; Becker, 1996; Garrido & Bodinier, 1999). These processes have obscured the original relationships with the host peridotites and modified their mineralogical and chemical compositions. It is therefore difficult to establish the precise origin of these rocks.

The Ronda peridotite also contains pyroxenites that cannot be interpreted either as crystal segregates in lithospheric dykes or as recycled oceanic crust (Garrido & Bodinier, 1999). These pyroxenites (spinel–plagioclase ± olivine websterites) occur only in the 'asthenospherized' part of the Ronda massif (Lenoir *et al.*, 2001; Vauchez & Garrido, 2001) [the 'coarse granular' and 'plagioclase-tectonite' domains of Van der Wal & Vissers (1996)], where they may locally predominate over the host lherzolites. They lack significant deformation and metamorphic imprint—except for some open folds and secondary plagioclase developed during the early stages of the exhumation of the massif, in the plagioclase–peridotite facies (Van der Wal & Vissers, 1996). The structural and textural features of these pyroxenites suggest an origin by pyroxene-forming, melt–rock reaction at near peridotite solidus conditions (Garrido & Bodinier, 1999). This resulted in localized replacement of refractory peridotites by spinel websterites. Based on recent observations in peridotite massifs, replacive pyroxenites may be widespread in the upper mantle (Bodinier & Godard, 2003). The mechanism of their formation has major implications for melt migration processes in the shallow mantle, as well as for the origin of veined and refertilized mantle. Because they have Mg-number [= Mg/(Mg + Fe) cationic ratio] values lower than 'pristine' mantle values ($<0{\cdot}89$), the existence of these pyroxenites also suggests that mantle melts can undergo substantial differentiation during their migration in the lithospheric mantle.

Further to constrain the formation of replacive pyroxenites in Ronda and better understand the reaction mechanisms suggested for their origin, we collected new samples for a detailed major- and trace-element study coupled with numerical simulation of melt–rock reaction processes. The interpretation that emerges from our data is a mechanism whereby the pyroxenites record channelling of uprising partial melts in (probably compaction-driven) high-porosity layers along the walls and top of the partial melting domain previously identified in the Ronda peridotite (Lenoir *et al.*, 2001).

GEOLOGICAL BACKGROUND

The Ronda orogenic peridotite

The Ronda massif (southern Spain; Fig. 1) is the largest (*c.* 300 km^2) of several orogenic peridotite massifs exposed

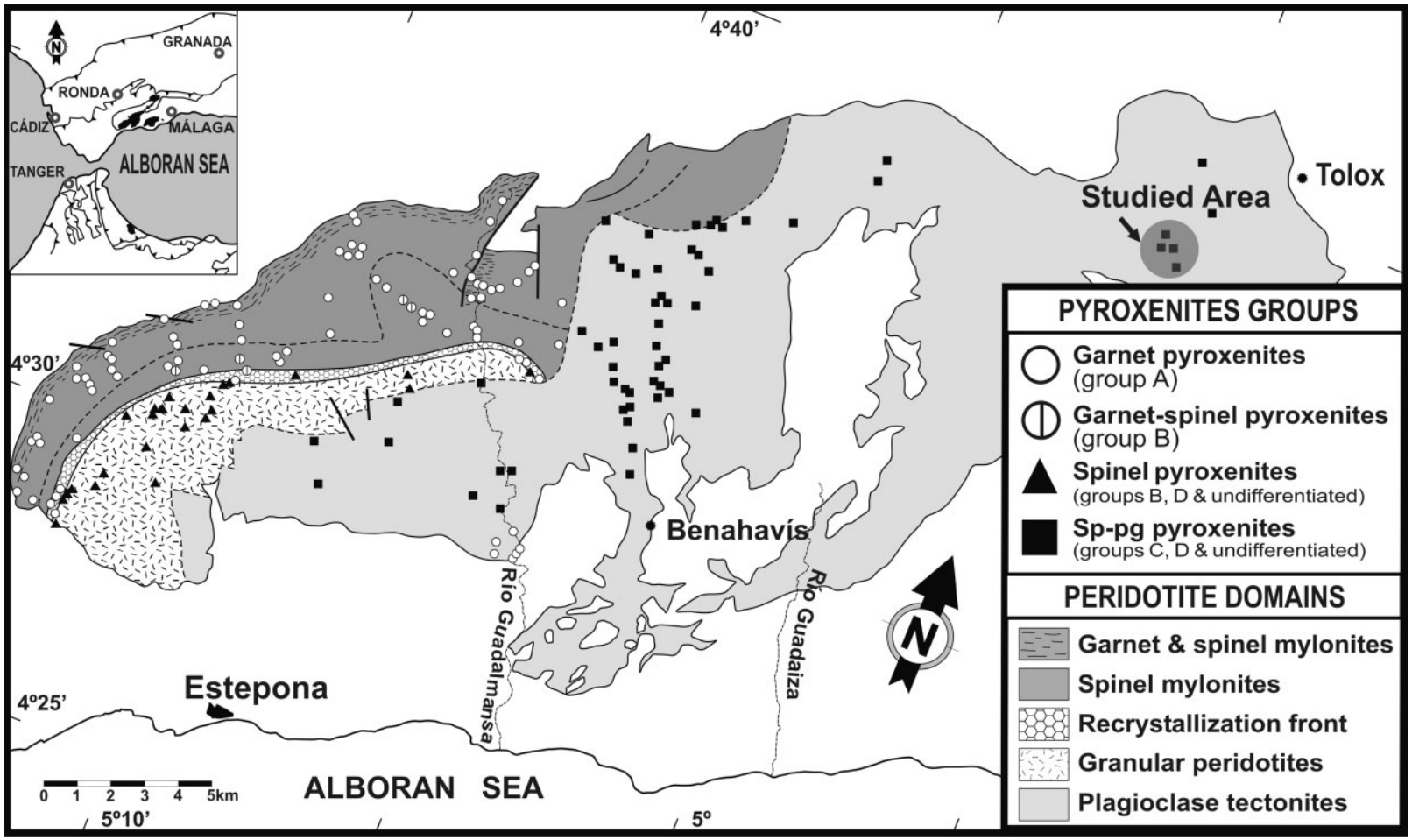

Fig. 1. Simplified geological map of the Ronda peridotite massif (southern Spain) showing the location of the study area in the easternmost part of the massif near the village of Tolox. Also shown are the different groups of pyroxenites mapped by Obata (1980) and Garrido & Bodinier (1999); the tectonic and metamorphic domains and the recrystallization front mapped by Van der Wal & Vissers (1996) and Lenoir *et al.* (2001); and the petrological facies boundaries mapped by Obata (1980). Inset shows the location of the Ronda massif within the realm of the Betic–Rif orogenic belt (southern Spain and northern Morocco).

in the Betic and Rif (northern Morocco) mountain belts in the westernmost part of the Alpine orogen. It was tectonically emplaced during early Miocene times in the internal zones of the Betic Cordillera. Several investigators have provided comprehensive reviews of the regional setting of the massif (Platt *et al.*, 2003; Booth-Rea *et al.*, 2005; Precigout *et al.*, 2007).

A first-order feature of the Ronda peridotite massif is its distinct kilometer-scale petrological, tectonic and geochemical zoning. From the NNW to the SSE of the massif, Obata (1980) mapped four metamorphic facies recording decreasing equilibrium pressure: (1) a garnet-lherzolite domain; (2) a spinel-lherzolite domain of the Ariegite sub-facies; (3) a spinel-lherzolite domain of the Seiland sub-facies; (4) a plagioclase-lherzolite domain. On the basis of overprinting relationships, Van der Wal & Vissers (1993, 1996) distinguished three tectonometamorphic domains of decreasing relative ages (Fig. 1), as follows.

(1) The spinel-tectonite domain corresponds to the garnet-lherzolite facies and the Ariegite sub-facies of Obata (1980). It is made of intensely foliated porphyroclastic spinel peridotites and mylonitic garnet–spinel peridotites (Precigout *et al.*, 2007), with subordinate amounts of garnet-bearing granulite and pyroxenite layers. The spinel tectonites represent an old lithospheric mantle, isolated from the convective mantle at 1·36 Ga (Reisberg & Lorand, 1995).

(2) The coarse granular peridotite domain broadly coincides with the Seiland sub-facies of Obata (1980). It is composed of virtually undeformed spinel peridotites and contains various types of pyroxenites, generally devoid of garnet. This domain is well exposed in the central part of the Ronda peridotite and occupies most of its western part. On the basis of structural and petrological criteria, Van der Wal & Bodinier (1996) subdivided the granular domain into three subdomains, namely, from NW to SE: (a) the 'coarse granular' subdomain, composed of homogeneous, coarse-grained harzburgites; (b) the 'fine granular' subdomain, dominated by less refractory, finer-grained, olivine-rich lherzolites; (c) the 'layered granular' subdomain, which shows a sequence of lherzolites, harzburgites, dunites and garnet-free pyroxenites.

(3) The plagioclase-tectonite domain is the youngest of the three tectonometamorphic domains recognized by Van der Wal & Vissers (1993, 1996). It is equivalent to the plagioclase lherzolite domain of Obata (1980) and is composed of porphyroclastic plagioclase peridotites, with subordinate mylonites and layers of spinel–plagioclase–olivine websterites. The development of this domain is related to the crustal emplacement of the massif and, therefore, overprints all magmatic and deformation structures observed in the other domains.

One of the most remarkable features of the Ronda massif is the 'recrystallization front' that represents the transition from the spinel-tectonite to the coarse granular peridotite domain (Fig. 1). Field, microstructural, petrological and geochemical evidence indicates that the recrystallization front represents the narrow boundary of a partial melting domain—caused by thinning and coeval asthenospheric upwelling—formed at the expense of former subcontinental lithospheric mantle and associated with melting and kilometer-scale migration of melts by diffuse porous flow through the 'asthenospherized' domain (Van der Wal & Vissers, 1993, 1996; Van der Wal & Bodinier, 1996; Lenoir *et al.*, 2001; Vauchez & Garrido, 2001). The evolution of the Ronda recrystallization front is considered as an example of thermal erosion and partial melting of subcontinental lithospheric mantle above upwelling asthenosphere. Across the front, which can be followed over a distance of almost 20 km in the massif (Fig. 1), all the structures of the 'lithospheric' spinel-tectonite domain were overprinted: the strongly foliated spinel tectonites were converted into coarse granular peridotites whereas garnet-bearing pyroxenite veins melted and recrystallized as garnet-free spinel websterites (Garrido & Bodinier, 1999). A few hundred meters ahead of the recrystallization–melting front, the presence of a more diffuse and irregular fertilization front—recorded by the precipitation of secondary clinopyroxene in the spinel tectonites—demonstrates that at least a smooth thermal gradient existed across the Ronda massif during the melting event. Therefore, the development and shape of the recrystallization front was probably thermally controlled. Differences in pyroxene compositions on either side of the front suggest a rapid, transient heating event at ~1200°C and ~1·5 GPa (Lenoir *et al.*, 2001). Behind the front, the strongly heterogeneous layered granular subdomain is considered to record melt redistribution and freezing while partial melting was receding upon conductive cooling of the massif (Van der Wal & Bodinier, 1996; Garrido & Bodinier, 1999). In this area, secondary lherzolites and layered spinel websterites formed by refertilization reactions are intermingled with anastomosed dunite bands interpreted as drainage channels for the last, evolved melt fractions (Gervilla & Remaïdi, 1993).

Pyroxenite types in the Ronda massif

On the basis of their structural and compositional characteristics, Garrido & Bodinier (1999) classified the Ronda pyroxenites into four groups. Group A comprises garnet-bearing rocks, interpreted either as mantle segregates or recycled oceanic crust, which occur only in the spinel-tectonite domain (Fig. 1). They form layers, isoclinally folded and/or boudinaged, parallel to the foliation of the spinel tectonites. Based on the presence of graphite pseudomorphs after diamonds (Davies *et al.*, 1993) and zircon ages significantly older than the age of massif exhumation (Sanchez-Rodriguez & Gebauer, 2000), these rocks are considered to represent the oldest pyroxenites lithologies recognized in Ronda. Group B is composed of strongly

deformed spinel websterites occurring along the recrystallization front. These pyroxenites were considered by Garrido & Bodinier (1999) to be formed at the expense of group A by melt–rock reaction with percolating melt in peridotites produced during the heating event. Group C comprises spinel (± plagioclase, ± olivine) websterites occurring only in the coarse granular domain (mostly in the layered subdomain; Gervilla & Remaïdi, 1993) and throughout the plagioclase-tectonite domain. The structural and textural features of these pyroxenites suggest an origin by metasomatic replacement of peridotites via a pyroxene-forming melt–rock reaction (Garrido & Bodinier, 1999). The waning stage of the melting event recognized in Ronda is marked by the formation of group D, Cr-rich pyroxenites. They occur mostly as composite layers with group A and B pyroxenites along the recrystallization front, and as single layers in the granular domain and in the plagioclase tectonites. Group D pyroxenites were formed by metasomatic replacement of previous pyroxenite layers by small fractions of refractory melts that percolated at a late stage throughout the massif. The last melt fractions were eventually tapped by cross-cutting dykes in the spinel-tectonite domain, indicating a final melt migration stage into cracks.

SAMPLING AND PETROGRAPHY OF GROUP C PYROXENITES

This study is focused on the genesis of group C pyroxenites, which comprise brownish spinel websterites and olivine–spinel websterites that contain variable amounts of plagioclase and were referred to as olivine gabbros in earlier studies (Obata, 1980; Suen & Frey, 1987). They are common throughout the Ronda layered granular subdomain and the plagioclase-tectonite domain (Fig. 1). In the field, group C pyroxenites are distinguished from the other Ronda pyroxenites by the lack of significant deformation, except for some open folds and secondary foliation coeval with the development of the plagioclase-tectonite domain.

The layered sequence sampled for this study is located in the easternmost part of the Ronda massif, near the village of Tolox (Fig. 1). This is a remarkable outcrop characterized by swarms of parallel layers or elongated lenses of spinel–plagioclase (± olivine) websterite and plagioclase lherzolite, a few centimeters to several tens of centimeters thick, intercalated with thin seams of olivine and locally minor dunite (Figs 2c and 3). The whole sequence is about 3 m thick and can be followed along-strike over several hundred meters in the field. As for other Ronda type C pyroxenites, the Tolox outcrop is characterized by gradual modal transitions—both across layering (Fig. 2b) and along strike (Fig. 2c)—from peridotites containing thin and rather diffuse pyroxenite layers (<1 cm), to olivine websterites (Fig. 2b), and to thick websterites lenses (>1 m) containing olivine seams (Fig. 2d). These gradual variations translate to a continuum of lithologies at outcrop scale ranging from lherzolites, to olivine websterites, and to websterites (Fig. 4).

The websterites have coarse granular to porphyroclastic textures, with brown clinopyroxene and orthopyroxene characterized by deformation twins and exsolution of counterpart pyroxenes. The lherzolites have coarse- to medium-grained granular microstructures with unevenly distributed and irregularly shaped clinopyroxene. Both in websterites and in lherzolites, spinel is rimmed by plagioclase (+ olivine) coronae; this feature suggests a subsolidus origin for plagioclase, associated with spinel breakdown (Obata, 1980). The amount of modal plagioclase varies from 5 to 25 vol.% in the studied samples. Where deformation and the metamorphic imprint are not pervasive, lherzolites and olivine-rich websterites show textures characterized by interstitial clinopyroxene, spinel and orthopyroxene armouring lobate olivine grains. These textures may be indicative of the precipitation of interstitial pyroxene + spinel, coeval with olivine dissolution.

We carried out serial sampling of 14 pyroxenites and peridotites (Fig. 3). Our main sampling goal was to retrieve fresh material for chemical analyses while covering the whole range of modal compositions available at the outcrop. The igneous modes of the Tolox peridotites and pyroxenites were reconstructed by mass balance of the whole-rock and mineral major element composition, using the total inversion method of Tarantola & Valette (1982). As the compositions of the Tolox pyroxenite minerals were strongly re-equilibrated in the plagioclase stability field, we used the compositions of minerals in other group C pyroxenites equilibrated in the spinel facies (Remaïdi, 1993). The results are reported in Table 1. On the olivine–orthopyroxene–clinopyroxene ternary diagram (Fig. 4), the Tolox pyroxenites show a wider range of modal variations, in term of pyroxene/olivine ratio, than previously reported for group C pyroxenites in the Ronda massif (Remaïdi, 1993; Garrido & Bodinier, 1999). The samples define a continuous trend marked by increasing pyroxene proportions, from 45–50% in lherzolites to >90% in the olivine-free websterites. This variation is associated with significant increase of the clinopyroxene/orthopyroxene ratio, from about 0·75 in lherzolites to 1·35 in websterites. The modal composition of the layered Tolox lherzolites approaches the field of massive Ronda peridotites unrelated to pyroxenite layering (Fig. 4). However, the Tolox lherzolites are distinguished by more fertile compositions, with 20–22 wt % clinopyroxene compared with ≤17 wt % in the other Ronda peridotites.

GEOCHEMISTRY

Analytical procedures

After crushing, sample aliquots were pulverized in a Pulverisette® agate mortar for solution analyses.

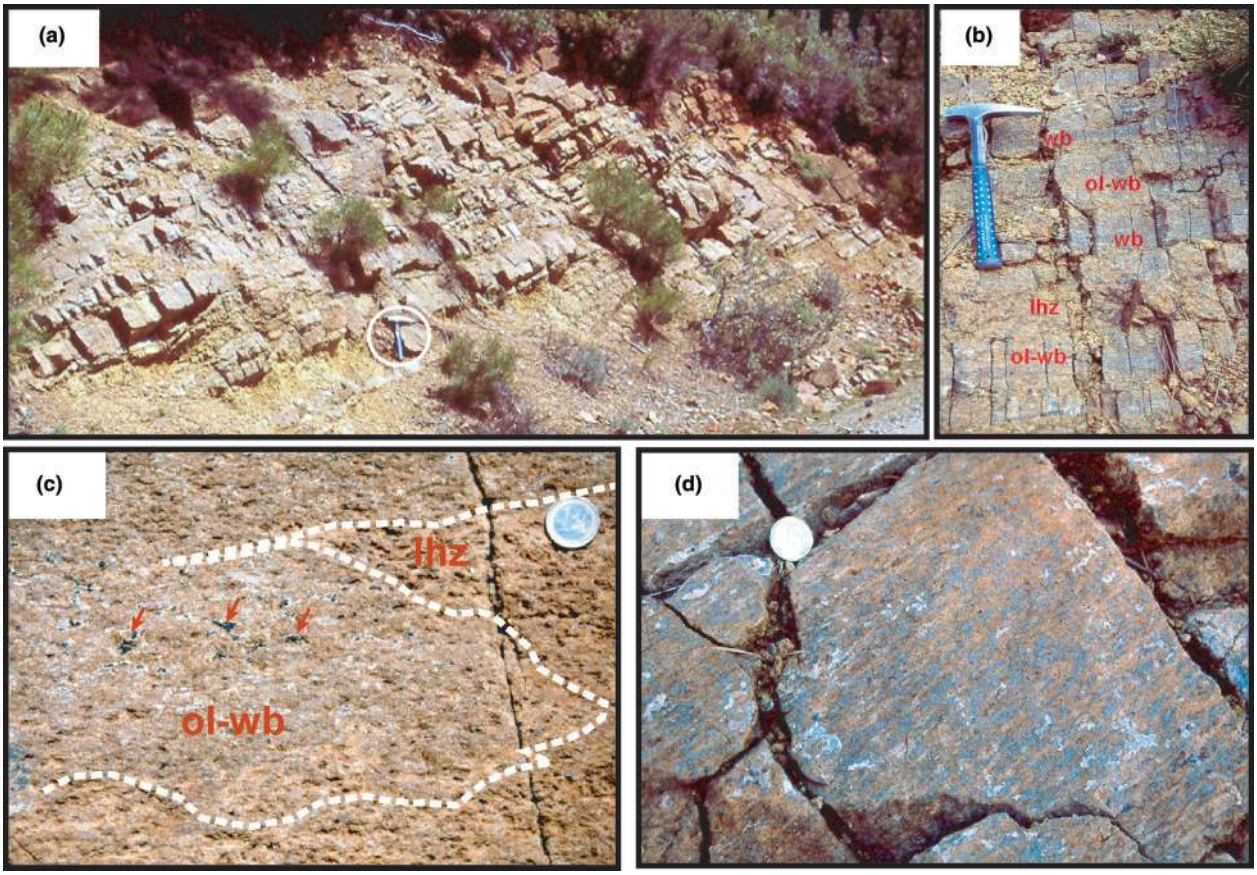

Fig. 2. Field photographs of the studied outcrop of layered spinel websterites near the village of Tolox. (a) Panoramic view of the outcrop showing the layered structure of the pyroxenite outcrop hosted in residual harzburgite–dunites and made up of the alternation of pyroxenitic and peridotitic lithologies. (b) Detailed view of the layered structure showing interbanded spinel websterite (wb), spinel–olivine websterite (ol-wb) and lherzolite (lhz). (c) Close-up view of the along-strike, gradual transition (dotted white line) from spinel–olivine websterite (ol-wb) to lherzolite (lhz). The red arrows point to coarse-grained spinel surrounded by sub-solidus plagioclase. (d) Detailed view of spinel–olivine websterite showing patchy, olivine-rich zones within websterite.

Major elements and Cr in whole-rocks were analyzed by inductively coupled plasma atomic emission spectrometry (ICP-AES) at CRPG (Nancy, France) following standard procedures. Minor and trace elements (Sc, V, Co, Ni, Cu, Rb, Sr, Y, Zr, Nb, Ba, REE, Hf, Ta, Pb, Th and U) in whole-rocks were analyzed by solution-ICP-MS (mass spectrometry). We used for sample dissolution the HF–$HClO_4$–HNO_3 digestion procedure described by Ionov *et al.* (1992). The analyses were run on a VG-PQ2 quadrupole instrument at Géosciences Montpellier (CNRS-Université de Montpellier II, Montpellier, France). Concentrations were determined by external calibration for most elements except Nb and Ta, which were calibrated by using Zr and Hf, respectively, as internal standards. This technique is an adaptation for ICP-MS analysis of the method described by Jochum *et al.* (1990) for the determination of Nb by spark-source mass spectrometry. This method avoids memory effects caused by the introduction of concentrated Nb–Ta solutions into the instrument. Detection limits obtained by long-term analyses of chemical blanks have been given by Garrido *et al.* (2000). Whole-rock data are reported in Table 1.

Major-element compositions of minerals were determined by electron probe microbeam analysis using a CAMECA SX100 at 'Microsonde Sud' facility (Montpellier, France). Analytical conditions were an accelerating voltage of 20 kV, a focused beam of 10 nA and counting times of 20–30 s. Several grains of each mineral were analysed to obtain representative averages and examine possible grain zoning. *In situ* trace element analyses of clinopyroxene were performed by laser ablation-ICP-MS on thick (*c.* 100 μm) sections with a VG-PQ2 ICP-MS system at Géosciences Montpellier coupled with a 193 nm Excimer laser ablation system (Compex 102). Primary output laser power was 160 mJ, pulse duration 25 ns and spot size 77 μm. Representative mineral analyses are reported in Tables 2 and 3.

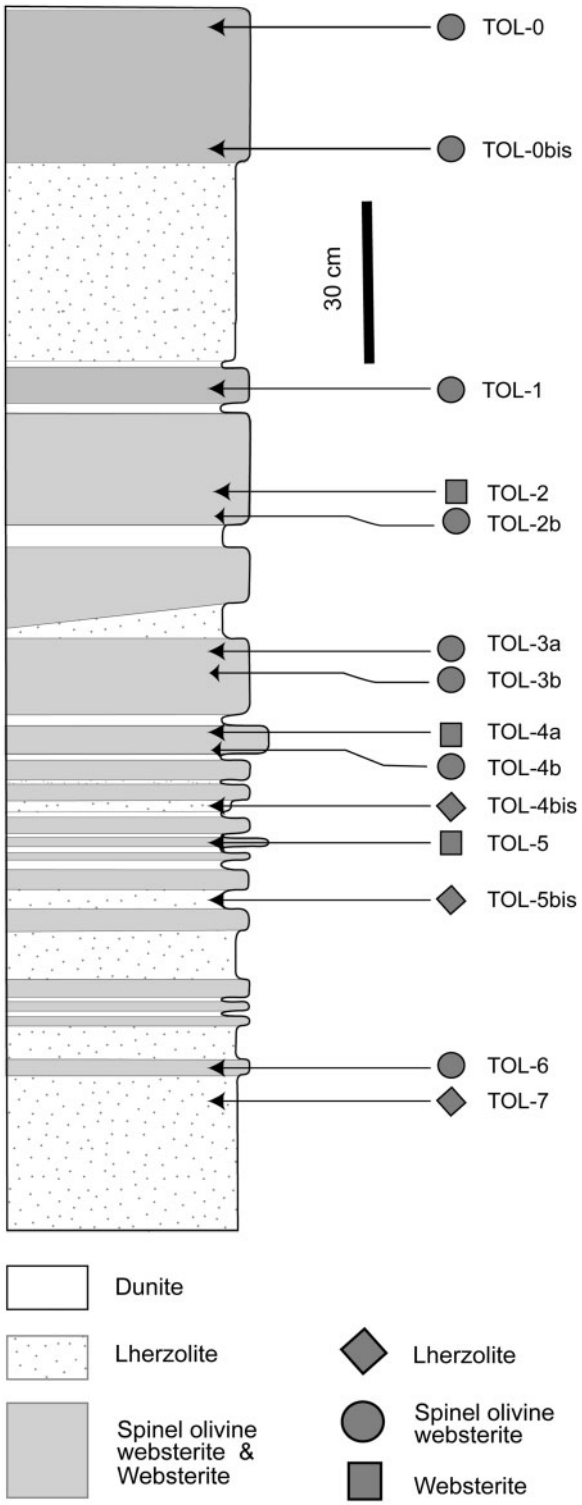

Fig. 3. Sketch of a cross-section of the Tolox layered pyroxenite–peridotite outcrop of Fig. 2, showing the alternation of peridotite and websterites, as well as the location and lithology of the samples selected for our study.

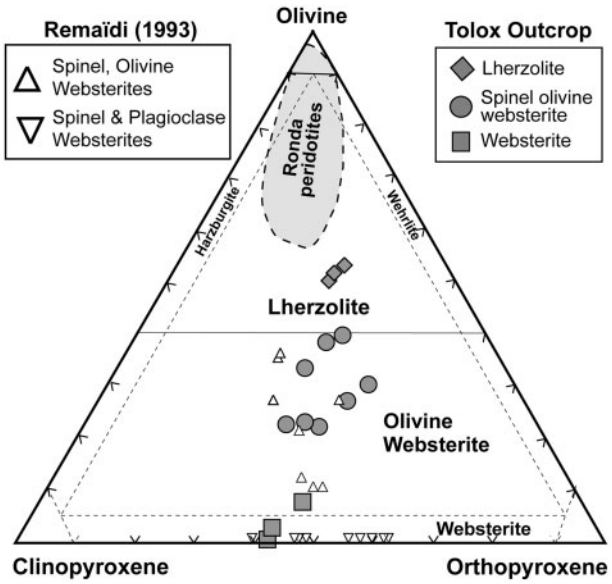

Fig. 4. Streckeisen triangular plot for the classification of ultramafic rocks, showing the primary modal composition of the Tolox pyroxenites and peridotites selected for this study. The primary composition of the Tolox samples was reconstructed in the Seiland subfacies by mass-balance computations using the whole-rock and mineral major element compositions (see text for further details on calculations). Also shown are group C spinel websterites from the layered coarse peridotite domain in the westernmost part of the Ronda peridotite (Remaïdi, 1993; Garrido & Bodinier, 1999), and the compositional field of Ronda peridotites (Remaïdi, 1993; Van der Wal & Bodinier, 1996).

Whole-rock compositions

Major elements

The websterites from Tolox are roughly similar in composition to the group C pyroxenites reported by Remaïdi (1993) and Garrido & Bodinier (1999), except for TiO_2, which is lower in the Tolox samples (Fig. 5). The studied pyroxenites are nevertheless markedly enriched in Ti compared with 'deformed' Ronda pyroxenites with similar mineralogical composition and MgO content (i.e. group B spinel websterites) (Fig. 5). This confirms the geochemical affinity of Tolox pyroxenites with Ronda group C websterites, as Ti enrichment is a distinctive signature of this pyroxenite group (Garrido & Bodinier, 1999).

As a whole, the Tolox section shows a wide range of major-element variation (e.g. 19·5–35·1 wt % MgO, 4·5–12·4 wt % Al_2O_3 and 4·2–12·4 wt % CaO) with strong inter-element correlations coupled with modal evolution. Al, Ca, Na and Ti steadily increase with decreasing Mg from lherzolites to olivine-free websterites (Fig. 5). Such covariations are typical of peridotite suites worldwide but are rarely observed in mantle pyroxenites (see, e.g. Ronda groups A and B in Fig. 5) (Bodinier & Godard, 2003). The compositional array defined by the Tolox samples fills the gap between Ronda peridotites and group A (garnet-bearing) pyroxenites, which represent the most 'evolved' type of pyroxenite in the massif in terms of SiO_2

Table 1: Whole-rock major and trace element composition of Tolox pyroxenite and peridotite

Rock type:	Olivine websterites								Websterites			Lherzolites		
Sample:	TOL-0	TOL-0bis	TOL-1	TOL-2B	TOL-3A	TOL-3B	TOL-4B	TOL-6	TOL-2	TOL-4A	TOL-5	TOL-4bis	TOL-5bis	TOL-7
Ol (wt %):	38	25	29	21	36	21	32	20	—	2	7	50	49	48
Opx (wt %):	33	39	41	33	30	32	30	36	40	39	41	26	26	26
Cpx (wt %):	25	30	25	37	28	42	34	35	55	54	45	18	20	22
Sp (wt %):	5	6	5	8	6	5	5	10	5	5	8	5	5	4
wt %														
SiO_2	45·66	47·78	48·46	45·32	44·22	46·72	44·85	47·16	48·76	48·17	47·45	43·84	44·98	45·14
TiO_2	0·38	0·48	0·43	0·47	0·35	0·52	0·37	0·56	0·64	0·58	0·54	0·27	0·35	0·36
Al_2O_3	7·12	9·09	7·54	9·69	7·30	7·70	6·64	11·06	10·55	10·22	12·35	4·51	5·37	6·01
FeO	8·23	6·89	7·63	7·95	9·23	7·67	9·31	6·08	6·26	6·95	6·15	10·36	8·31	7·55
MnO	0·14	0·14	0·15	0·14	0·14	0·14	0·14	0·14	0·15	0·15	0·17	0·14	0·11	0·13
MgO	31·32	27·30	28·40	26·08	30·79	26·09	29·41	25·70	19·52	20·14	21·58	35·07	34·76	34·41
CaO	5·65	6·78	5·78	8·43	6·31	9·39	7·56	7·72	12·35	12·02	10·10	4·22	4·67	4·98
Na_2O	0·51	0·78	0·66	0·97	0·63	0·82	0·64	0·83	0·99	0·93	0·90	0·36	0·53	0·54
K_2O	<b.d.l.	<b.d.l.	<b.d.l.	<b.d.l.	<b.d.l.	<b.d.l.	<b.d.l.	<b.d.l.	<b.d.l.	<b.d.l.	<b.d.l.	<b.d.l.	<b.d.l.	<b.d.l.
P_2O_5	0·07	<b.d.l.	0·11	0·06	<b.d.l.	0·08	0·05	0·07	0·08	0·07	0·07	0·08	<b.d.l.	0·05
LOI	0·64	0·35	0·21	0·72	1·08	0·74	0·61	0·50	0·34	0·24	0·48	1·51	1·61	1·47
Sum	100·37	100·39	100·12	100·72	100·69	100·44	100·10	100·99	100·30	100·00	100·49	101·01	101·60	101·37
Mg-no.	87·1	87·6	86·9	85·4	85·6	85·8	84·9	88·3	84·7	83·7	86·2	85·7	88·1	89·0
ppm														
Sc	20·1	28·8	23·0	30·4	22·7	29·2	28·7	28·4	44·7	44·2	36·9	16·1	17·1	19·7
Ti	2801	2977	2798	3201	2447	3454	2840	3562	4426	4181	3723	1734	2390	2479
V	154	179	161	200	153	195	186	175	260	267	199	102	117	129
Cr	2220	2765	2575	3020	2160	1890	1805	4000	2230	1835	2390	2240	3130	2515
Ni	1776	1246	1099	1103	1719	1417	1595	1036	771	940	653	1286	1248	2168
Cu	65	61	36	10	72	131	67	49	82	108	48	39	40	44
Co	84	59	63	71	91	69	94	53	45	56	43	108	92	92
Rb	0·11	0·51	0·55	0·23	0·17	0·76	0·17	0·66	0·58	0·47	0·60	0·05	0·15	0·10
Sr	13·23	19·84	28·66	51·21	25·27	36·96	32·79	48·37	63·09	49·86	30·81	18·31	23·41	29·17
Y	11·72	13·56	9·54	11·42	9·65	12·85	7·53	11·42	17·46	12·91	11·87	5·47	6·41	6·49
Zr	18·23	21·17	16·50	21·62	15·72	28·35	15·39	26·56	31·19	25·62	20·45	10·86	13·91	17·80
Nb	0·028	0·032	0·039	0·068	0·032	0·054	0·070	0·070	0·112	0·135	0·057	0·033	0·034	0·040
Ba	0·51	2·91	0·50	0·13	0·45	0·39	0·49	0·50	0·15	0·26	0·70	0·04	0·16	0·23
La	0·214	0·283	0·361	0·71	0·427	0·78	0·69	0·80	1·10	0·96	0·448	0·375	0·356	0·492
Ce	1·29	1·57	1·63	2·78	1·81	3·35	2·57	3·24	4·33	3·84	2·10	1·35	1·54	2·11
Pr	0·36	0·42	0·36	0·55	0·39	0·67	0·52	0·63	0·87	0·76	0·49	0·30	0·32	0·43
Nd	2·47	2·82	2·30	3·22	2·31	3·99	2·96	3·63	5·09	4·39	3·25	1·77	1·95	2·48
Sm	1·10	1·26	0·97	1·21	0·91	1·44	0·99	1·23	1·90	1·56	1·32	0·61	0·75	0·85
Eu	0·439	0·508	0·392	0·484	0·372	0·555	0·381	0·495	0·744	0·614	0·535	0·244	0·306	0·322
Gd	1·71	2·05	1·50	1·78	1·39	2·07	1·35	1·82	2·80	2·19	1·91	0·86	1·10	1·14
Tb	0·320	0·375	0·266	0·312	0·249	0·360	0·229	0·322	0·489	0·381	0·343	0·146	0·191	0·190
Dy	2·35	2·70	1·91	2·21	1·80	2·48	1·57	2·29	3·43	2·67	2·37	1·02	1·32	1·31
Ho	0·506	0·578	0·403	0·465	0·385	0·519	0·328	0·485	0·726	0·557	0·501	0·220	0·277	0·282
Er	1·42	1·61	1·14	1·28	1·08	1·43	0·90	1·39	2·04	1·60	1·45	0·64	0·78	0·79
Tm	0·212	0·237	0·168	0·180	0·156	0·206	0·127	0·201	0·296	0·229	0·213	0·091	0·111	0·116

(continued)

Table 1: Continued

Rock type:	Olivine websterites								Websterites			Lherzolites		
Sample:	TOL-0	TOL-0bis	TOL-1	TOL-2B	TOL-3A	TOL-3B	TOL-4B	TOL-6	TOL-2	TOL-4A	TOL-5	TOL-4bis	TOL-5bis	TOL-7
Ol (wt %):	38	25	29	21	36	21	32	20	—	2	7	50	49	48
Opx (wt %):	33	39	41	33	30	32	30	36	40	39	41	26	26	26
Cpx (wt %):	25	30	25	37	28	42	34	35	55	54	45	18	20	22
Sp (wt %):	5	6	5	8	6	5	5	10	5	5	8	5	5	4
Yb	1·37	1·53	1·09	1·12	1·00	1·31	0·80	1·26	1·83	1·42	1·34	0·57	0·68	0·72
Lu	0·226	0·247	0·179	0·176	0·163	0·208	0·130	0·207	0·293	0·225	0·221	0·095	0·107	0·120
Hf	0·816	0·929	0·680	0·731	0·596	0·932	0·556	0·926	1·100	0·876	0·810	0·382	0·558	0·632
Ta	0·0006	0·0012	0·0030	0·0086	0·0033	0·0095	0·0063	0·0110	0·0136	0·0135	0·0052	0·0025	0·0031	0·0058
Pb	0·057	0·027	0·022	0·010	0·046	0·071	0·064	0·035	0·048	0·069	0·025	0·036	0·018	0·054
Th	0·0006	0·0006	0·0011	0·0041	0·0013	0·0033	0·0040	0·0042	0·0077	0·0091	0·0026	0·0012	0·0020	0·0026
U	0·0005	0·0009	0·0008	0·0014	0·0010	0·0015	0·0024	0·0014	0·0029	0·0030	0·0012	0·0010	0·0252	0·0013

Ol, olivine; Cpx, clinopyroxene; Opx, orthopyroxene; Sp, spinel; LOI, loss on ignition; b.d.l., below detection limit.

and Al_2O_3 contents (Garrido & Bodinier, 1999). At the most 'depleted' end of the Tolox array, the lherzolites plot near the inferred composition of Primitive Upper Mantle, which coincides with the composition of the most fertile orogenic peridotites [e.g. sample R717 from Ronda of Frey *et al.* (1985)]. At the most 'fertile' end of the array, olivine-free websterites approach the composition of group A mafic layers. In contrast with element abundances, the Mg-number is poorly correlated with modal variations (not shown), but the highest value (0·890) is nevertheless observed in a lherzolite and the lowest one (0·837) in an olivine-free websterite (Table 1).

Minor and trace elements

Similar to major elements, the minor transition elements show covariations with MgO and modal compositions comparable with those observed in several suites of mantle peridotites worldwide (Fig. 6). Their compositional range also covers the gap between Ronda peridotites and group A mafic layers. Like Ti (Fig. 5), the incompatible elements Sc and V increase with decreasing MgO from lherzolites to olivine-free websterites whereas the compatible elements Ni and Co decrease. The middle and heavy rare earth elements (MREE and HREE; Sm and Yb, respectively; Fig. 7) are negatively correlated with MgO and steadily increase from lherzolites to olivine-free websterites. The light rare earth elements (LREE), Zr, Hf and Sr are more dispersed when plotted versus MgO, but nevertheless show significant increase from lherzolites to olivine-free websterites (e.g. Ce and Zr in Fig. 7). In contrast, the highly incompatible trace elements Cs, Rb, Ba, Th, U, Nb and Ta (as well as Pb) are not correlated with MgO and lack significant variations according to rock types.

As noted above, Garrido & Bodinier (1999) pointed to Ti enrichment as a distinctive feature of group C pyroxenites compared with other types of Ronda pyroxenites (Fig. 5). Group C pyroxenites are in fact strongly enriched in all moderately incompatible minor and trace elements compared with other mafic layers with similar MgO content (Figs 5–7). Relative to the composition of group B spinel websterites, the enrichment factor is a maximum for Ti and MREE (e.g. a factor of three for Sm), as well as for Zr and Hf, which have comparable peridotite/melt partition coefficients (Figs 5–7). The less (HREE, Y, Sc, and V) and more (LREE) incompatible elements are less enriched. Both compatible and highly incompatible elements are either comparable with group B in composition (Ni, Nb, Ta, U, Rb) or more depleted (Co, Th, Ba).

The Tolox samples have REE concentrations mostly in the range of 1–10 times chondrite abundances (Fig. 8). Similar to the vast majority of Ronda pyroxenites and their host peridotites, they are impoverished in normalized LREE relative to MREE and HREE ($La_N/Yb_N = 0{\cdot}14–0{\cdot}5$). However, like other group C pyroxenites (Remaïdi, 1993; Garrido & Bodinier, 1999), the Tolox websterites (and the associated lherzolites) are distinguished from the other Ronda pyroxenites by convex-upward normalized REE patterns. This feature further illustrates the selective enrichment of Tolox samples and group C pyroxenites in the moderately incompatible elements MREE, Ti, Zr and Hf, compared with less and more incompatible elements. This signature is reflected in MREE/LREE and MREE/HREE ratios both higher than one (e.g. $Sm_N/La_N = 2{\cdot}2–7{\cdot}7$ and $Gd_N/Yb_N = 1{\cdot}03–1{\cdot}4$). Finally, it should be noted that the Tolox samples do not

Table 2: Major element composition of minerals and REE contents in clinopyroxenes

	TOL-0 (olivine websterite)					TOL-4a (websterite)				TOL-5 (websterite)				
	Ol	Sp	Opx	Cpx ($n=9$)	Pg	Ol	Opx	Cpx ($n=17$)	Pg	Ol	Sp	Opx	Cpx ($n=19$)	Pg
wt %														
SiO_2	40·5		54·29	51·22 ± 0·54	47·66	39·83	55·00	51·3 ± 0·39	49·74	40·42		55·33	49·85 ± 0·70	48·33
TiO_2		1·91	0·42	1·32 ± 0·18			0·31	1·03 ± 0·13			0·218	0·441	1·55 ± 0·30	
Al_2O_3		26·19	4·39	3·85 ± 0·48	33·1		2·47	3·74 ± 0·47	31·96		55·22	2·30	4·87 ± 0·77	32·56
Cr_2O_3		34·30	0·36	0·66 ± 0·08			0·214	0·407 ± 0·06			7·34	0·222	0·374 ± 0·11	
FeO	13·71	26·61	8·98	3·81 ± 0·34		17·02	11·08	4·79 ± 0·41		13·89	18·02	9·24	4·05 ± 0·23	
MnO	0·21	0·30	0·23	0·12 ± 0·01		0·26	0·29	0·15 ± 0·02		0·315	0·20	0·353	0·18 ± 0·02	
MgO	45·11	10·52	30·43	15·72 ± 0·53		42·79	29·75	15·3 ± 0·35		45·26	17·72	31·05	15·16 ± 0·34	
CaO	0·031		0·80	22·5 ± 0·6	16·34	0·03	0·75	22·5 ± 0·7	14·99	0·029		0·855	22·3 ± 0·8	15·71
Na_2O			0·02	0·51 ± 0·04	2·37		0·013	0·52 ± 0·03	3·24			0·017	0·617 ± 0·09	2·79
NiO	0·375	0·191	0·09	0·04 ± 0·01		0·32	0·076	0·03 ± 0·02		0·188	0·225	0·041	0·02 ± 0·01	
Total	99·97		99·77	99·74	99·47	100·28	99·88	99·74	100·25	100·13	99·06	99·84	99·14	
Mg-no.	0·85	0·41	0·86	0·88 ± 0·01		0·82	0·83	0·85 ± 0·01		0·85	0·64	0·86	0·87 ± 0·01	
Cr-no.		0·47									0·08			
An					0·79				0·72					0·76
				($n=20$)				($n=14$)					($n=11$)	
ppm														
La				0·37 ± 0·06				1·4 ± 0·17					0·512 ± 0·05	
Ce				3·3 ± 0·6				5·3 ± 0·7					3·2 ± 0·4	
Pr				1·41 ± 0·28				1·5 ± 0·19					1·2 ± 0·2	
Nd				11 ± 2				8·8 ± 1					9·3 ± 1·5	
Sm				5·1 ± 0·9				3·1 ± 0·4					4·4 ± 1·0	
Eu				1·4 ± 0·3				1·07 ± 0·1					1·30 ± 0·2	
Gd				7·4 ± 1·3				4·2 ± 0·5					6·7 ± 1·6	
Tb				1·30 ± 0·25				0·69 ± 0·09					1·2 ± 0·3	
Dy				9·5 ± 1·9				4·8 ± 0·6					8·5 ± 1·9	
Ho				2·0 ± 0·4				0·96 ± 0·14					1·8 ± 0·4	
Er				5·4 ± 1·1				2·7 ± 0·4					5·2 ± 1·2	
Tm				0·76 ± 0·15				0·37 ± 0·05					0·73 ± 0·17	
Yb				4·8 ± 0·9				2·4 ± 0·4					4·7 ± 1·0	
Lu				0·64 ± 0·1				0·34 ± 0·06					0·7 ± 0·1	

(continued)

exhibit positive Eu anomalies despite the presence of substantial amounts of plagioclase (5–25%) (Fig. 8). This feature is consistent with textural evidence indicating a subsolidus origin for plagioclase.

Normalized to Primitive Mantle (PM) abundances, the minor and trace elements show subtle negative anomalies of Y, Zr and Sr relative to neighbouring REE (Fig. 9). The highly incompatible elements Ba, Th, U, Nb and Ta are strongly depleted relative to LREE, with Ba, Th and U values mostly in the range 0·01–0·1 × PM, and Nb–Ta in the range 0·01–0·3 × PM. Extremely low abundance of these elements compared with LREE (e.g. $Th_N/La_N = 0·02–0·04$) is typical of Ronda group C pyroxenites (Garrido & Bodinier, 1999). The alkaline elements Cs and Rb are selectively enriched relative to other highly incompatible elements, a feature that is shared by most mafic layers and peridotites in Ronda. Concentrations of Cs and Rb are comparable with PM values.

Mineral compositions

Significant variations of mineral compositions as a function of whole-rock modal and chemical compositions are

Table 2: Continued

	TOL-5bis (lherzolite)				TOL-6 (olivine websterite)			
	Ol	Sp	Opx	Cpx ($n=8$)	Ol	Opx	Cpx ($n=6$)	Pg
wt %								
SiO_2	40·51		55·57	50·33 ± 0·80	40·46	54·99	49·79 ± 1·28	47·93
TiO_2		0·279	0·411	1·54 ± 0·27		0·496	1·63 ± 0·31	
Al_2O_3		45·99	2·28	4·74 ± 0·90		2·8	4·67 ± 0·95	32·65
Cr_2O_3		17·11	0·431	0·895 ± 0·10		0·412	0·594 ± 0·10	
FeO	11·85	17·76	7·82	3·34 ± 0·21	11·66	7·77	3·27 ± 0·34	
MnO	0·19	0·18	0·19	0·09 ± 0·02	0·237	0·224	0·12 ± 0·02	
MgO	47·2	16·53	32·0	15·31 ± 0·51	47·09	32·16	15·23 ± 0·57	
CaO	0·02		0·68	22·7 ± 0·4	0·035	0·702	22·8 ± 0·5	16·03
Na_2O			0·01	0·629 ± 0·07		0·008	0·628 ± 0·13	2·75
NiO	0·373	0·252	0·073	0·03 ± 0·02	0·368	0·104	0·04 ± 0·01	
Total	100·19	98·21	99·99	99·57	99·90	99·67	99·36	99·57
Mg-no.	0·88	0·62	0·88	0·89 ± 0·01	0·88	0·88	0·89 ± 0·01	
Cr-no.		0·20						
An								0·76
				($n=14$)			($n=10$)	
ppm								
La				1·3 ± 0·3			1·4 ± 0·4	
Ce				6·1 ± 1·5			7·8 ± 1·5	
Pr				1·9 ± 0·5			2·5 ± 0·4	
Nd				13 ± 3			16 ± 2	
Sm				5·1 ± 1·1			6·2 ± 0·9	
Eu				1·6 ± 0·3			1·8 ± 0·3	
Gd				7 ± 2			8·4 ± 1·1	
Tb				1·2 ± 0·3			1·4 ± 0·2	
Dy				8 ± 2			10·3 ± 1·6	
Ho				1·7 ± 0·4			2·1 ± 0·3	
Er				4·5 ± 1·1			5·6 ± 0·8	
Tm				0·61 ± 0·15			0·7 ± 0·1	
Yb				3·8 ± 0·8			4·8 ± 0·7	
Lu				0·5 ± 0·1			0·7 ± 0·1	

observed only for the Mg-number in silicates and the Cr content of pyroxenes (Table 2). The olivine forsterite content (Fo), for instance, decreases from 0·88 in the analyzed lherzolite to 0·85–0·88 in olivine websterites and 0·82–0·85 in olivine-free websterites. Similarly, the clinopyroxene Cr_2O_3 content decreases from 0·9 wt % in the lherzolite to 0·59–0·66 wt % in olivine websterites, and 0·37–0·41 wt % in olivine-free websterites (Table 2). Some mineral compositions, however, do not vary according to rock type, but rather as a function of plagioclase proportion, thus reflecting the degree of mineral re-equilibration in the plagioclase stability field. This is typically the case for Cr-number [= Cr/(Cr + Al) cationic ratio] in spinel, which shows a wide variation (0·08–0·47) irrespective of modal composition (Table 2), but to a lesser extent also for Al in pyroxenes (e.g. Al_2O_3 in orthopyroxene = 2·3–4·4 wt %) and HREE in clinopyroxene. Finally, some elements do not show significant variations, either according to rock type or as a function of plagioclase proportion (e.g. Na in clinopyroxene and Ti in ortho- and clinopyroxene).

The chondrite-normalized REE patterns of clinopyroxene (Fig. 10) resemble those of the whole-rocks (Fig. 8). However, the clinopyroxenes are distinguished by higher MREE/LREE and MREE/HREE ratios

Table 3: Selected LA-ICP-MS analyses of the REE content (ppm) of clinopyroxenes lacking Eu anomalies

Sample:	TOL-4a	TOL-4a	TOL-4a	TOL-4a	TOL-4a	TOL-4a	TOL-4a	TOL-5	TOL-5	TOL-6
La	1·43	1·26	1·40	1·61	1·66	1·61	1·48	0·51	0·58	1·82
Ce	5·35	4·80	5·22	5·96	6·59	5·77	5·11	3·00	3·15	8·7
Pr	1·46	1·30	1·27	1·51	1·89	1·63	1·41	0·95	1·11	2·30
Nd	8·8	7·6	8·3	8·8	10·5	10·0	7·9	7·5	7·2	12·9
Sm	3·20	2·66	2·69	2·87	3·59	3·20	2·48	2·99	2·78	4·33
Eu	1·10	0·95	1·04	1·04	1·43	1·24	1·09	1·12	1·21	1·46
Gd	4·36	3·59	4·06	3·50	5·24	4·36	3·64	4·79	4·04	5·46
Tb	6·56	5·36	6·16	6·21	8·7	8·2	6·09	8·5	6·64	8·8
Dy	4·72	3·83	4·16	4·29	5·94	5·73	3·94	5·91	5·52	6·43
Ho	0·99	0·73	0·89	0·81	1·21	1·14	0·77	1·22	1·18	1·25
Er	2·67	2·02	2·29	2·24	3·36	3·09	2·45	3·66	3·49	3·49
Tm	0·38	0·28	0·34	0·32	0·48	0·42	0·37	0·46	0·54	0·56
Yb	2·67	1·75	2·16	2·08	3·05	2·87	2·70	3·40	3·52	3·82
Lu	0·38	0·25	0·29	0·31	0·46	0·42	0·35	0·49	0·58	0·50
EuN/Eu*	0·90	0·94	0·96	1·00	1·01	1·01	1·10	0·90	1·10	0·91
$(Sm/Yb)_N$	1·33	1·70	1·38	1·53	1·31	1·24	1·02	0·98	0·88	1·26
$(Ce/Nd)_N$	0·46	0·48	0·48	0·52	0·48	0·44	0·50	0·31	0·33	0·51

$Eu^* = 2 \times Eu_N/(Sm + Gd)_N$; N indicates chondrite normalized after Sun & McDonough (1989).

($Sm_N/La_N = 3{\cdot}4$–$22{\cdot}2$ and $Gd_N/Yb_N = 1{\cdot}1$–$1{\cdot}5$). Their normalized REE patterns are therefore even more convex in shape than those of the whole-rocks. The LREE and HREE contents and the LREE/HREE and LREE/MREE ratios may significantly vary between two samples from a given rock type (e.g. $La_N/Yb_N = 0{\cdot}078 \pm 0{\cdot}003$ and $0{\cdot}42 \pm 0{\cdot}09$, respectively in the two websterite samples), but no significant difference is observed between rock types. Some clinopyroxenes from websterites (and one clinopyroxene in an olivine websterite) are devoid of a Eu anomaly but the majority display a negative anomaly. A point worthy of note is that the HREE content of clinopyroxene tends to be correlated with the amplitude of the negative Eu anomaly. Yb_N does not exceed 20 in clinopyroxenes without significant Eu anomaly [$(Eu_N/Eu^*$ in the range $0{\cdot}9$–$1{\cdot}1$; $Eu^* = (Sm_N + Gd_N)/2$] but increases up to 40 in those showing an Eu negative anomaly. This feature may reflect the subsolidus re-equilibration of clinopyroxene with metamorphic plagioclase.

DISCUSSION

Genesis of group C pyroxenites

Magmatic, metamorphic and metasomatic origins have been successively postulated for the origin of Ronda group C pyroxenites. Similar to other Ronda pyroxenites, they were first interpreted as igneous crystal segregates crystallized in magma conduits (Suen & Frey, 1987). Parental picritic melts were ascribed to high degrees of partial melting in the inner part of a mantle diapir in the model envisioned by Obata (1980). In this scenario, group A and B pyroxenites were interpreted as crystal segregates from more evolved melts that migrated from the inside towards the colder outside of the mantle diapir. Thereafter, on the basis of the structural overprinting relationships observed in the host peridotites, Van der Wal & Vissers (1996) considered group C mafic layers as the result of metamorphic re-equilibration of group A and B garnet pyroxenites in the plagioclase stability field. Finally, on the basis of field, structural and geochemical evidence, Garrido & Bodinier (1999) showed that group C pyroxenites are not cogenetic with group A and B layers and suggested their formation by metasomatic replacement of peridotites via a melt-consuming, melt–peridotite reaction. This process was ascribed to the receding stages of the melting domain bounded by the Ronda recrystallization front.

Our new geochemical data confirm that Tolox layered pyroxenites belong to group C pyroxenites. Especially striking in the Tolox outcrop is the wide range of compositions observed in a single swarm of layers, with modal and chemical compositions varying between two end-members (Figs 4–7): (1) lherzolites only slightly more fertile than Primitive Mantle and the most fertile lherzolites unrelated to layering in Ronda; (2) olivine-free websterites approaching the composition of the 'evolved' group A mafic layers (Figs 5–7). Three mechanisms may potentially account for this variability, as follows.

(1) Variable degrees of mechanical dispersion of pyroxenite (olivine-free websterite) in peridotite (host harzburgite or dunite) (Allègre & Turcotte, 1986; Becker, 1996). This process can be ruled out in Tolox (as well as in most of the granular and plagioclase-tectonite domains in Ronda), as the pyroxenites and peridotites are virtually undeformed.

(2) Variable degrees of partial melting and melt extraction from a former pyroxenite protolith (olivine-free websterite). This mechanism is suggested by the similarity of the Tolox element covariations trends with those observed in peridotite suites worldwide, which are classically ascribed to partial melting (e.g. Frey *et al.*, 1985, for Ronda). However, partial melting is not consistent with the constant Ti and Na values observed in pyroxenes from various lithologies (Table 2), as well as with the lack of correlation between several inter-element ratios (e.g. LREE/HREE) and modal compositions. Moreover, the observed textures are at odds with the melting model, as they indicate precipitation of interstitial pyroxene + spinel. Group C pyroxenites affected by partial melting

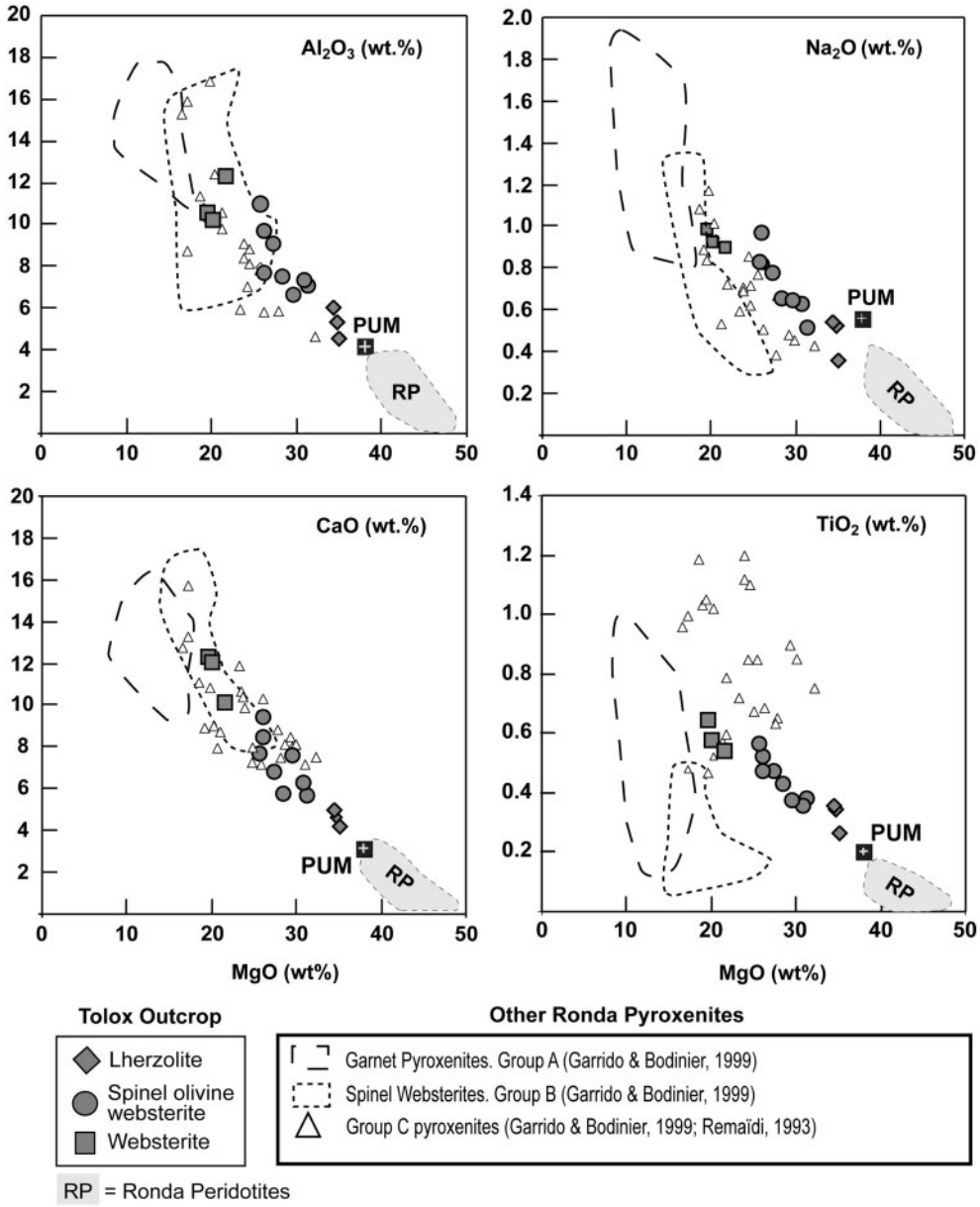

Fig. 5. Covariation diagrams of MgO concentration (wt %) vs concentration of selected major elements (Al_2O_3, CaO, Na_2O and TiO_2, in wt %) in Tolox pyroxenites and peridotites, compared with the compositional field of Ronda garnet pyroxenites and deformed spinel websterites, corresponding to pyroxenite groups A and B, respectively, of Garrido & Bodinier (1999). Also shown are group C spinel websterites from the layered coarse peridotite domain in the westernmost part of the Ronda peridotite (Remaïdi, 1993; Garrido & Bodinier, 1999), and the compositional field of Ronda peridotites (Remaïdi, 1993; Van der Wal & Bodinier, 1996). PUM, Primitive Upper Mantle (Palme & Jones, 2003).

(or dunite-forming melt–rock reaction) have been identified in the southwestern part of Ronda (in the layered granular subdomain; Gervilla & Remaïdi, 1993; Remaïdi, 1993) and were classified as group D layers by Garrido & Bodinier (1999). However, these rocks are markedly different from the Tolox olivine websterites and lherzolites. Their modal composition is dominated by orthopyroxene (up to 40%) + olivine and their normalized REE patterns are mostly U-shaped (Gervilla & Remaïdi, 1993).

(3) Variable degrees of refertilization of a peridotite protolith (host harzburgite or dunite) by percolating melt. This process may occur via three mechanisms, although all transitions are expected between these extremes: (a) entrapment and *in situ* crystallization of interstitial

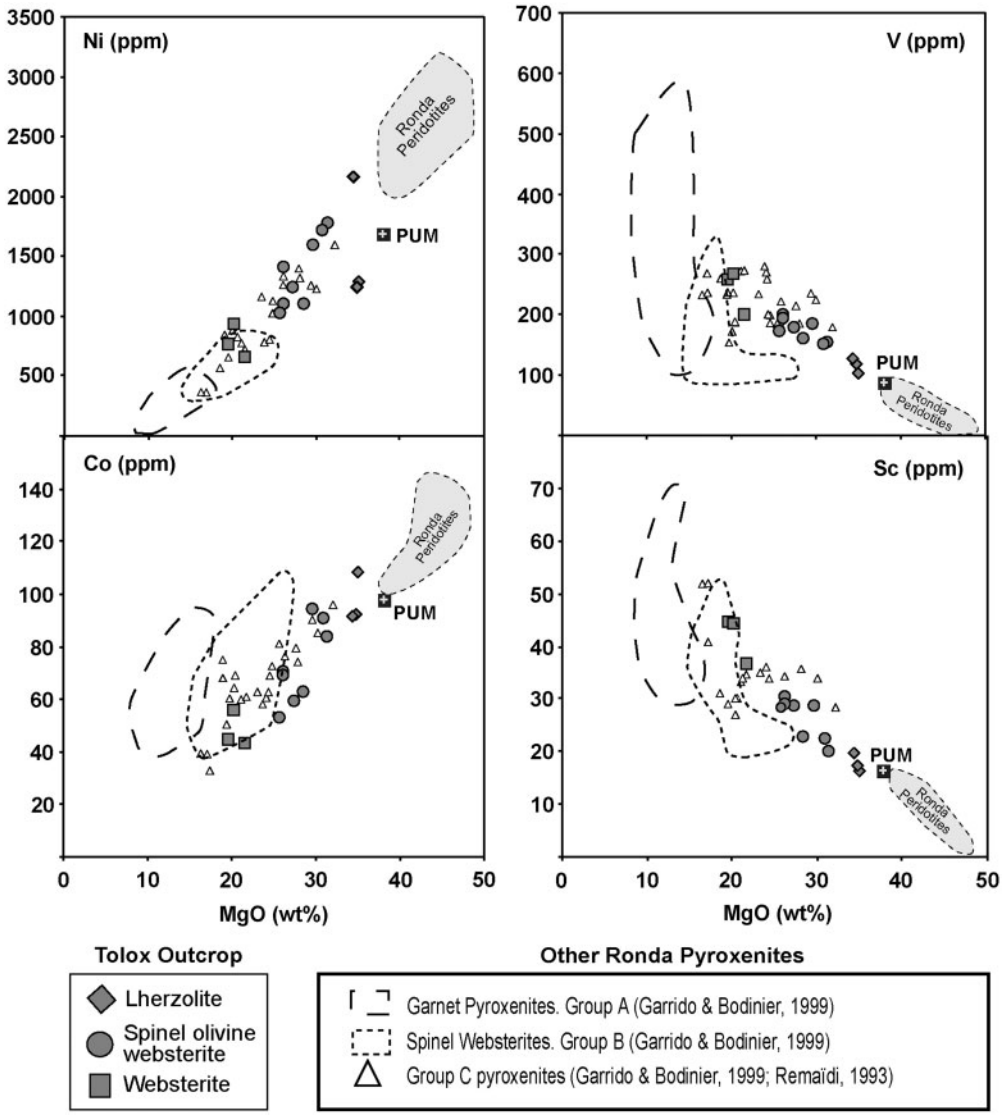

Fig. 6. Covariation plots of MgO concentration (wt %) vs concentration of selected minor elements (Ni, Co, V and Sc, in ppm) in Tolox pyroxenites and peridotites, compared with the compositional field of Ronda garnet pyroxenites and deformed spinel websterites, corresponding to pyroxenite groups A and B, respectively, of Garrido & Bodinier (1999). Also shown are group C spinel websterites from the layered coarse peridotite domain in the westernmost part of the Ronda peridotite (Remaïdi, 1993; Garrido & Bodinier, 1999), and the compositional field of Ronda peridotites (Remaïdi, 1993; Van der Wal & Bodinier, 1996). PUM, Primitive Upper Mantle (Palme & Jones, 2003).

melt ['melt impregnation' process of Obata & Nagahara (1987) and Rampone *et al.* (1997)]; (b) interstitial crystallization of pyroxene + spinel segregates from percolating melt [the 'percolative fractional crystallization' process of Harte *et al.* (1993)]; (c) peritectic, melt-consuming reaction between peridotite and percolating melt involving olivine dissolution and precipitation of pyroxene + spinel (Kelemen *et al.*, 1992); in this last model, interstitial space for pyroxene + spinel precipitation can be created, at least partly, by olivine dissolution, whereas models (a) and (b) require localized volume expansion, most probably driven by concomitant compaction of partially molten peridotites (Maaløe & Scheie, 1982; McKenzie, 1984; Obata & Nagahara, 1987).

Although refertilization by melt entrapment [model (a)] represents a viable mechanism under certain circumstances, it can be ruled out for Ronda group C pyroxenites because of their strong depletion in Ba, Th and U relative to LREE (Fig. 9). Because of their low concentrations, the ratios of highly incompatible elements in mixtures of peridotite + trapped melt are readily imposed by the melt component (e.g. Sharma *et al.*, 1995). Ratios such as Th/La in the Tolox samples display values (0·0032–0·0095) that are lower than most depleted mantle melts (0·048 for

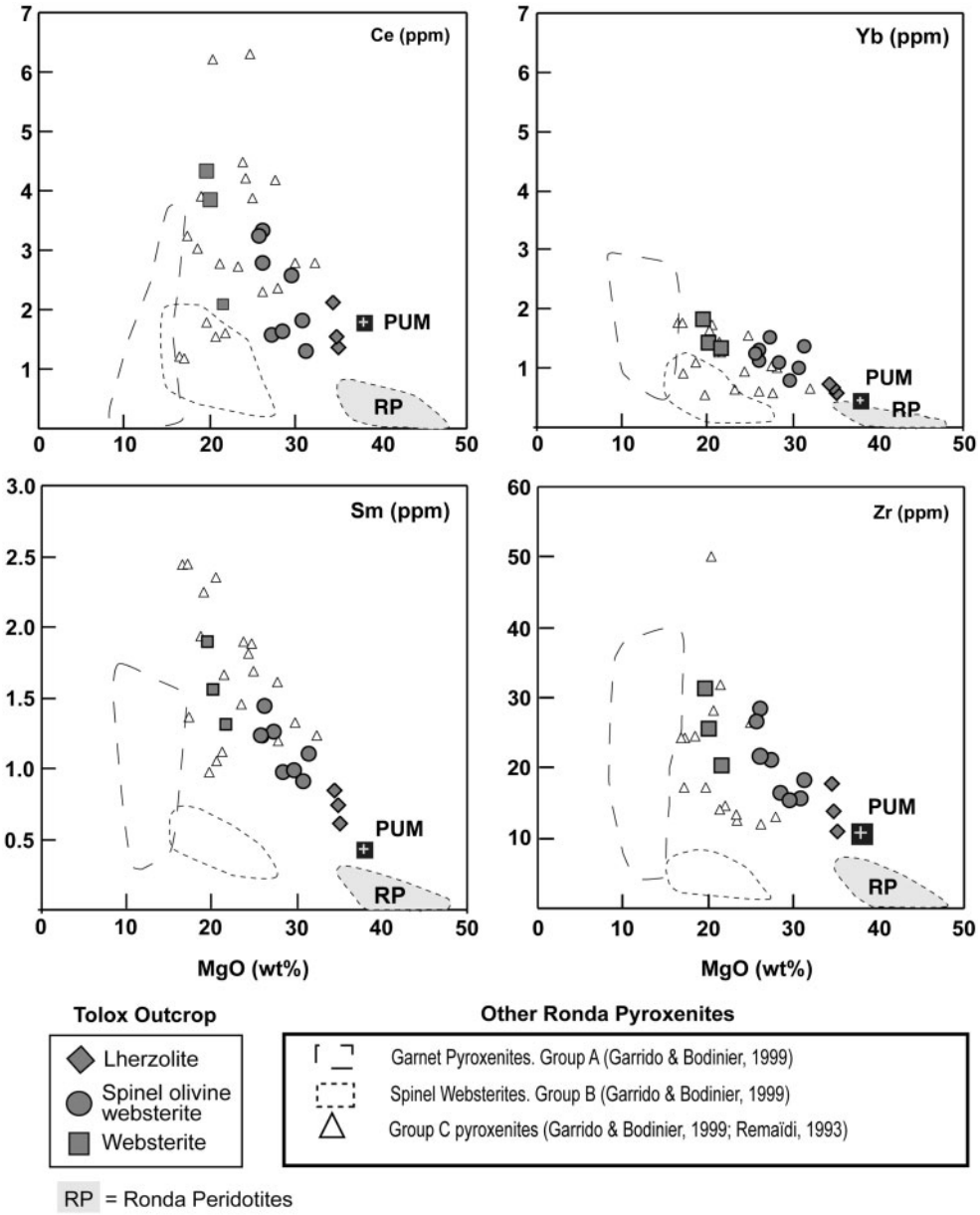

Fig. 7. Covariation plots of MgO concentration (wt %) vs concentration of selected trace elements (Ce, Sm, Yb and Zr, in ppm), compared with the compositional field of Ronda garnet pyroxenites and deformed spinel websterites, corresponding to pyroxenite groups A and B, respectively, of Garrido & Bodinier (1999). Also shown are group C spinel websterites from the layered coarse peridotite domain in the westernmost part of the Ronda peridotites (Remaïdi, 1993; Garrido & Bodinier, 1999), and the compositional field of Ronda peridotites (Remaïdi, 1993; Van der Wal & Bodinier, 1996). PUM, Primitive Upper Mantle (Palme & Jones, 2003).

N-MORB; Sun & McDonough, 1989). This clearly indicates that igneous refertilization in Tolox did not occur via melt entrapment. A similar conclusion was reached by Koga *et al.* (2001) for peridotites 'impregnated' by clinopyroxene + plagioclase in the Oman ophiolite on the basis of Eu distribution between these minerals. No such straightforward evidence allows us to discriminate between the two other refertilization models. In addition, structural and textural observations indicate that both mineral precipitation in open spaces and olivine dissolution probably occurred, suggesting that the actual process was transitional between models (b) and (c).

Further constraints on refertilization mechanisms can be retrieved from the Mg-number variation and the trace-element signature of the Tolox samples. Because significant Mg-number variations in mantle porous flow

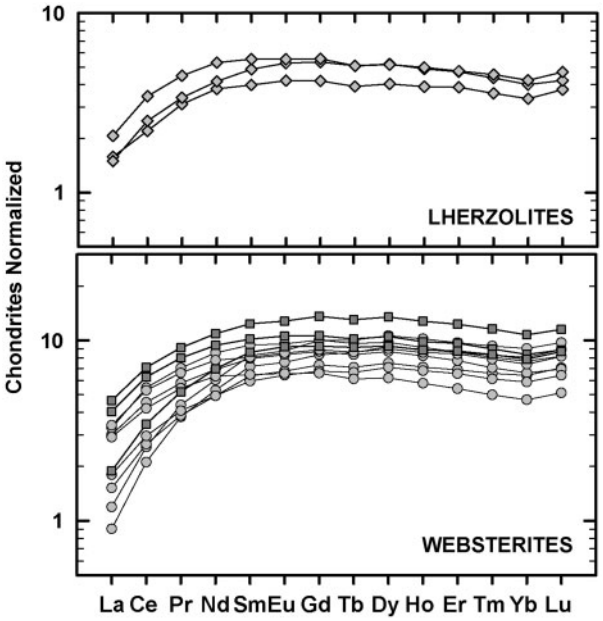

Fig. 8. Chondrite-normalized REE patterns of Tolox lherzolites (upper panel) and Tolox olivine spinel websterites and spinel websterites (lower panel). Normalizing values after Sun & McDonough (1989). Symbols are as in Fig. 3.

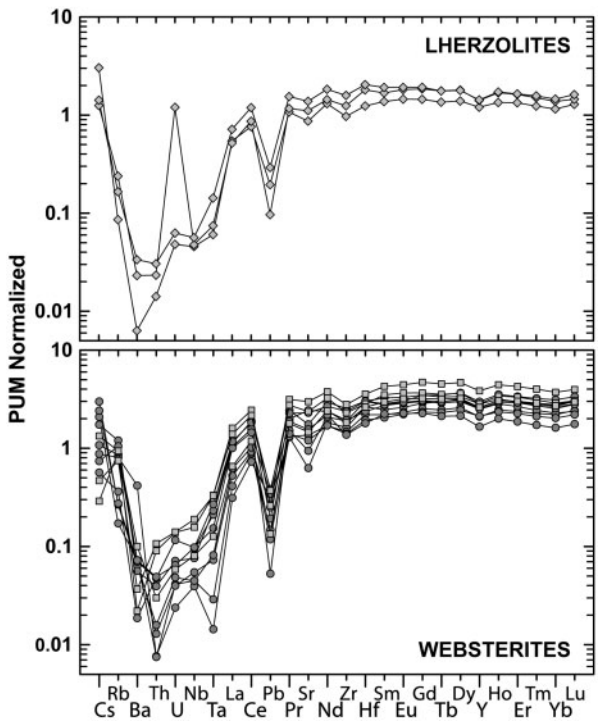

Fig. 9. Primitive upper mantle-normalized patterns of incompatible trace elements of Tolox lherzolites (upper panel) and Tolox olivine spinel websterites and spinel websterites (lower panel). Normalizing values after Sun & McDonough (1989). Symbols are as in Fig. 3.

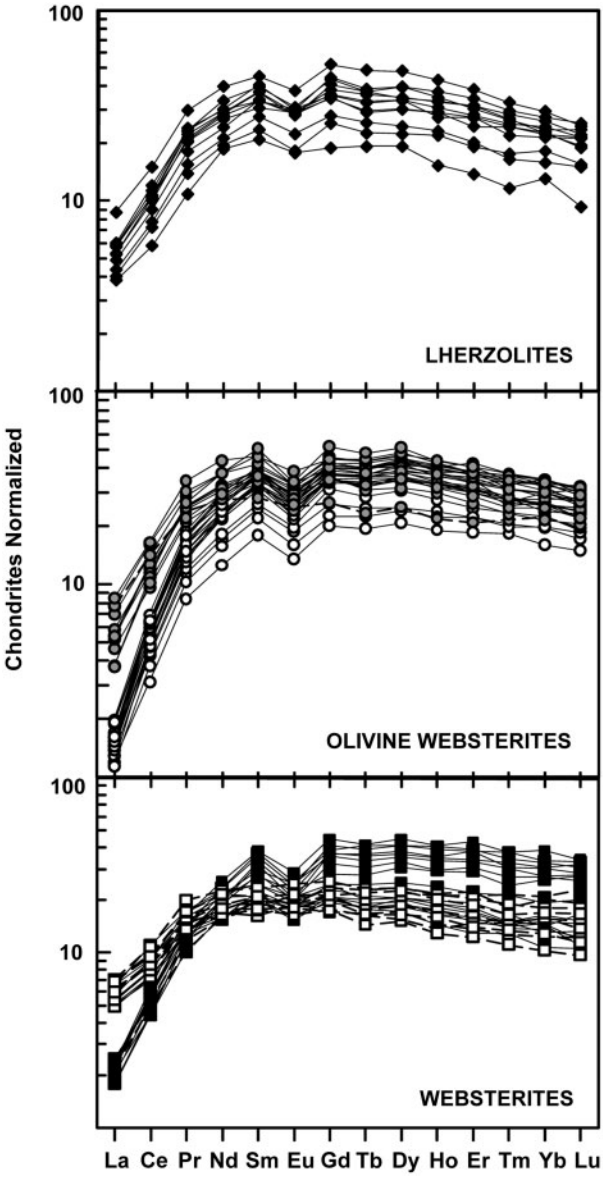

Fig. 10. Chondrite-normalized REE patterns of clinopyroxenes from a lherzolite, two olivine websterites and two websterites from Tolox (◆, lherzolite sample TOL-5bis; ○, olivine websterite sample TOL-0; grey circles, olivine websterite sample TOL-6; □, websterite sample TOL-4a; ■, websterite sample TOL-5). Samples lacking a significant Eu anomaly [Eu_N/Eu^* in the range 0·9–1·1; $Eu^* = (Sm_N + Gd_N)/2$] are distinguished by dashed lines. Normalizing values after Sun & McDonough (1989).

systems are hampered by Mg–Fe buffering by silicate minerals, notably olivine (Bedini *et al.*, 2002; Ionov *et al.*, 2005), decreasing Mg-number with increasing refertilization (Fo = 0·88–0·83 from lherzolites to olivine-free websterites) is a strong indication that the percolating melt underwent substantial fractional crystallization, olivine dissolution was limited and the layers were formed at high melt/rock ratio. This favours the percolative

fractional crystallization process [model (b)] rather than a melt/rock reaction in a strict sense [model (c)]. This conclusion at first sight conflicts with the trace-element signature of the studied samples, as percolative fractional crystallization is generally associated with extreme enrichment of LREE and highly incompatible elements (Bedini *et al.*, 1997; Bodinier *et al.*, 2004). In contrast, the studied samples are depleted in LREE relative to HREE (Figs 8 and 10) and strongly impoverished in highly incompatible elements (Ba to Ta in Fig. 9).

The one-dimensional theoretical approach of Godard *et al.* (1995) provides a key to solve the paradox of decreasing Mg-number without concomitant increase of highly incompatible element abundances. Those workers have examined the coupled geochemical effects of melt transport and melt–rock reaction in a porous flow column. They showed that the amplitude and spatial location (in the column) of trace-element anomalies resulting from the sink or source effects of a reaction strongly depends, at a given reaction rate, on chromatographic effects governed by the peridotite/melt partition coefficients of the elements and the Darcy flux in the column, hence of the time-integrated melt/rock ratio. This effect was verified by Vernières *et al.* (1997) with a numerical simulation of trace-element redistribution associated with reactive porous flow (the 'Plate Model'). Of particular interest for the genesis of Ronda group C pyroxenites is that the enrichment of incompatible elements at low melt/rock ratio (atop the percolation column) is displaced to the less incompatible elements—such as MREE and Ti—at higher melt/rock ratios (i.e. lower in the column; see Vernières *et al.*, 1997, fig. 9).

In the following, we first report the results of a numerical simulation using the Plate Model of Vernières *et al.* (1997) applied to Mg-number variations. The aim is to evaluate whether the observed covariation of Mg-number and modal proportions can be explained by reactive igneous refertilization. Then, the Plate Model is used to reproduce the convex shape of the normalized REE patterns in group C clinopyroxenes with the inferred refertilization process. Our purpose is primarily to explain the enrichment of moderately incompatible elements coupled with a strong depletion of highly incompatible elements in the studied samples. We used the REE composition of clinopyroxene as a proxy for the whole trace-element signature. Although peridotite/melt partition coefficients for REE vary within a narrower range than those for an extended set of trace elements, REE show convex-upward normalized patterns (i.e. enrichment of MREE relative to both LREE and MREE) that we assume to be representative of the whole trace-element signature. However, the clinopyroxene REE compositions potentially have been modified by subsolidus equilibration with plagioclase. This effect is therefore evaluated before modelling REE variations related to reactive porous flow.

Numerical simulation of Mg-number variations

Model setup

Our approach is based on the Plate Model proposed by Vernières *et al.* (1997) for the simulation of trace-element fractionation during partial melting and reactive porous flow in the Earth's upper mantle. This model was adapted to the simulation of Fe–Mg redistribution in peridotite–melt systems by Bedini *et al.* (2002). Details of the procedure have been reported by Ionov *et al.* (2005). As discussed by Hanson & Langmuir (1978), Mg and Fe can be considered as trace elements during melt–rock interaction processes—hence a 'K_d approach' can be applied for modelling—as long as the stoichiometry of the solid phases is respected (e.g. the sum MgO + FeO must be kept constant at 66·67 mol% in olivine). In turn, the mineral stoichiometry imposes strong limitations on the extent of Mg–Fe exchange between solid and liquid phases. To avoid mineral stoichiometry violation, the total inverse method of Tarantola & Valette (1982) is used to constrain Mg–Fe redistribution between solid and liquid phases after each reaction increment. The model parameters are *a priori* values for the inversion; they are fixed within variable confidence intervals, depending on how well they are constrained by experimental and/or analytical data.

The model was applied to a reaction process involving precipitation of clinopyroxene (cpx) + orthopyroxene (opx) at the expense of interstitial melt + olivine (ol). Spinel is not taken into account for Mg-number modelling. The mechanism of percolative fractional crystallization is considered as a limiting case of this reaction scheme where no olivine is dissolved. Mg and Fe mineral/melt partitions coefficients were fixed after Ulmer (1989) for a pressure of 1·5 GPa and a temperature of 1250°C. They are allowed to vary during numerical experiments to account for Mg and Fe variations in the melt, based on experimental constraints (Ulmer, 1989). For the 'parallel approach' of Vernières *et al.* (1997), the reaction takes the general form

$$\begin{aligned}\phi\,\mathrm{Liq}_0 + F(1-\phi)\mathrm{Ol} \rightarrow &\left[f\phi + F(1-\phi)\right]\mathrm{Liq}_\mathrm{r} \\ &+ (1-f)\phi\, q_\mathrm{opx}\mathrm{Opx} \\ &+ (1-f)\phi\, q_\mathrm{cpx}\mathrm{Cpx} \qquad (1)\end{aligned}$$

where Liq_0 and Liq_r stand for the infiltrated and residual (= 'reacted') melts, respectively, ϕ for residual fraction of infiltrated melt at the onset of a reaction increment (for simplicity ϕ is referred to as 'porosity' in the following), F for the mass fraction of dissolved olivine (relative to the initial solid matrix), f for the mass fraction of residual melt (relative to the initial porosity) and q_opx and q_cpx for the crystallized mass fractions of opx and cpx. Reactions at

decreasing melt mass require that $f\phi + F(1 - \phi) < \phi$, which implies

$$\frac{F}{(1 + F - f)} < \phi. \quad (2)$$

Based on the average composition of the coarse granular domain (Lenoir *et al.*, 2001), the protolith affected by the reaction is considered to be an olivine-rich lherzolite (70·6 wt % olivine, 21·4 wt % opx and 8·0 wt % cpx). Provided that a sufficient amount of melt is available for the reaction, the formation of olivine-free websterite from a harzburgite protolith may be accounted for by multiple combinations of ϕ, F and f in reaction (1). We performed several experiments to evaluate the effect of the model parameters and found that the covariations of Mg-number and modal compositions are best monitored by the melt/rock ratio, that is, the porosity (ϕ) values integrated over the range of increments for a given reaction run, and the mass ratio of crystallized minerals to infiltrated melt (R). For the parallel reaction scheme of Vernières *et al.* (1997), R is simply given by

$$R = 1 - f. \quad (3)$$

ϕ and F were arbitrarily fixed at 0·1 and 0·001, respectively, whereas f was adjusted to allow variations of R. The q_{opx} and q_{cpx} values were constrained by modal proportions in the olivine-free websterites and fixed at 0·4 and 0·6, respectively. With the fixed ϕ and F values, the olivine-free websterite modal composition can be obtained within a single run after <1000 reaction increments. Other sets of parameters (e.g. involving lower porosity values: $\phi < 0{\cdot}1$) may require several runs to produce the olivine-free websterite because the porosity will close as a result of interstitial melt crystallization. However, as long as the infiltrated melt composition is kept constant, the results obtained with these approaches do not significantly differ from those obtained with a single run.

Model results

The numerical experiment 1 shown in Fig. 11a involves continuous infiltration of 'primitive' melt (Mg-number = 0·745) in equilibrium with the harzburgite protolith. This model produces only a slight decrease of the Mg-number towards the pyroxenite (0·89 in the olivine-free websterite, compared with 0·904 in the harzburgite). This result is not surprising as Mg–Fe variations in this model are strongly buffered by both the host peridotite minerals and the continuous infiltration of primitive melt. At high melt/rock ratios (>1) the effect of the reaction is counterbalanced by that of melt infiltration, resulting in roughly constant Mg-number values. However, this first model involving continuous infiltration of primitive melt is clearly unrealistic. Whatever the main direction of melt transport during the formation of the Tolox layers—perpendicular to layering as in the compaction models of Obata & Nagahara (1987), or mostly along strike as in the channelling model of Garrido & Bodinier (1999)—the reaction probably involved melts that were already differentiated as a result of earlier reaction stages. However, the composition of melt fractions involved during the formation of a given layer is unknown. We can

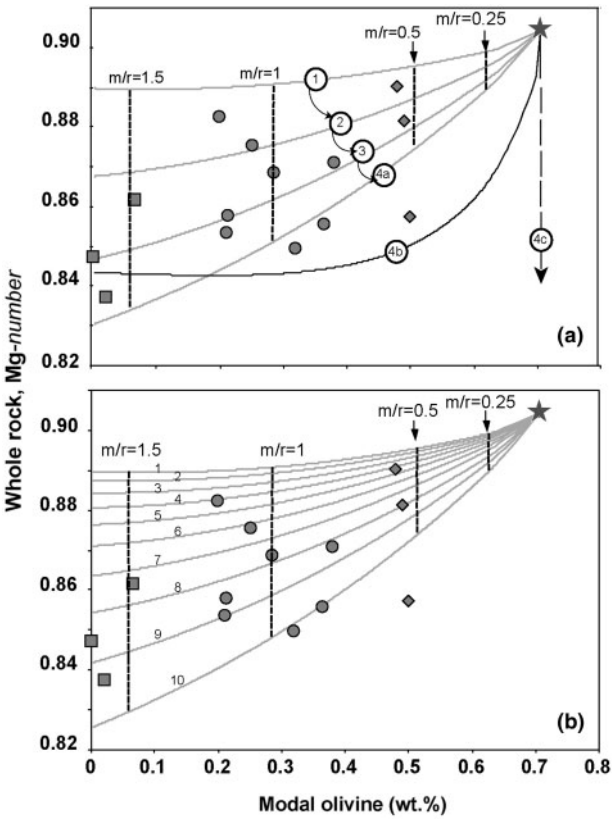

Fig. 11. Variation of the whole-rock Mg-number [Mg-number = Mg/(Mg + Fe) atomic ratio] vs modal content of olivine (wt %) for Tolox peridotites and pyroxenites, compared with the results of different numerical experiments of Mg-number variations produced by interaction of a refractory harzburgite (star, Mg-number = 0·9043; olivine wt % = 0·70) with different types of incoming melt in two sets of numericalsimulations. (a) Set of numerical experiments where experiment 1 shown involves continuous infiltration of 'primitive' melt (Mg-number = 0·745) in equilibrium with the harzburgite protolith. The numbers on the curves refer to different numerical experiments. For experiments 2–4, we modelled a multi-stage process whereby the protolith is successively infiltrated and reacted with the evolved melt resulting from previous, pyroxene-forming reaction stages. In experiment 2 (curve 2), the original harzburgite protolith is infiltrated by reacted melt in equilibrium with the final olivine-free websterite of experiment 1. Similarly, the infiltrated melt of experiments 3 and 4a are the reacted melts of experiments 2 and 3, respectively. (b) Set of numerical experiments where the composition of the infiltrated melt of stage $n+1$ is calculated by mixing reacted melt from stage n with melt in equilibrium with the harzburgite protolith (= infiltrated melt of stage 1). The numbers on the curves refer to the consecutive nth runs. In both sets of numerical models the m/r values on the vertical lines indicate the melt/rock ratio. (See text for further details on the significance of the numerical model parameters.)

only guess that it lies in the interval between the value of primitive melt in equilibrium with the harzburgite protolith (0·745) and that of melt in equilibrium with the most differentiated pyroxenite (~0·68).

To evaluate the effect of reaction with evolved melts, we used a simplified multi-stage approach whereby the protolith is successively infiltrated by (and reacts with) evolved melt resulting from previous, pyroxene-forming reaction stages. In run 2 (Fig. 11a), the unmodified, original harzburgite protolith is infiltrated by reacted melt in equilibrium with the final olivine-free websterite of experiment 1. Similarly, the infiltrated melts of experiments 3 and 4a are the reacted melts of experiments 2 and 3, respectively. With this model, most of the Tolox compositions may be accounted for by melt/rock ratios in the range 0·5–1·7 and R values around 0·5 ($f = 0{\cdot}5$). A few samples characterized by low Mg-number values at relatively high olivine proportions can be fitted either by increasing the number of runs in the model (>4) or by decreasing R (i.e. the crystallization rate). Experiment 4b, for instance, was run with the same parameters as experiment 4a, except for a lower R value (= 0·1). Experiment 4c shows the result of a pure percolation model ($R = 0$). We also ran experiments starting from modally and chemically modified peridotites (as a result of previous reaction stages) rather than from the original, unmodified harzburgite. However, this approach (not shown in Fig. 11) does not significantly change our results in terms of melt/rock ratios and R values.

Between the extreme situations depicted in Fig. 11a by experiment 1 (infiltration of primitive melt) and experiments 2–4 (infiltration of evolved melt), transitional situations may involve infiltration of mixed, primary and evolved melts. Garrido & Bodinier (1999) suggested the formation of group C pyroxenites by refraction and channelling of upwelling partial melt atop a partial melting domain (Sparks & Parmentier, 1991; Spiegelman, 1993; Rabinowicz & Ceuleneer, 2005). In this model, melt channels are continuously supplied by new fractions of partial melt from a molten peridotite source. Inspired by this model, we ran a second set of numerical experiments where the composition of the infiltrated melt of stage $n+1$ is calculated by mixing reacted melt from stage n with melt in equilibrium with the harzburgite protolith (= infiltrated melt of stage 1). The result of this model is shown in Fig. 11b. In this model the contribution of reacted melt to the infiltrated melt composition increases by steps of 10%, from 0% at stage 1 to 90% at stage 10. The results are similar to those obtained with the model involving the infiltration of pure reacted melts (runs 2–4 in Fig. 11a), except for the number of runs, which must be greater to reach the lower Mg-number values observed in the Tolox samples.

The models shown in Fig. 11a and b involve melt compositions that are variable between runs but constant within a single run. More sophisticated models involving variable compositions of infiltrated melt during a single run are beyond the scope of this study, mostly because variations of melt composition cannot be constrained. In addition, this approach would merely result in different shapes of the Mg-number vs modal olivine covariation curves (Fig. 11), but it would hardly change our results in terms of melt/rock ratios and R values. Our results confirm that the genesis of Ronda group C pyroxenites implies high melt/rock ratios and substantial fractional crystallization of the percolating melt. Above all, Mg-number modelling indicates that most of the studied samples were formed at the expense of melts that were already differentiated as a result of previous reaction stages. This indicates that melt flow probably occurred mostly parallel to layering. Altogether, these results are consistent with formation of group C layers in high-porosity porous-flow channels.

Subsolidus REE redistribution in clinopyroxene

Although they may contain large amount of plagioclase (up to 25%), Tolox pyroxenites are devoid of positive Eu anomalies in whole-rock REE patterns (Fig. 8). Combined with the existence of negative Eu anomalies in clinopyroxenes (Fig. 10), this feature may be explained either by: (1) entrapment of interstitial melt crystallized as plagioclase + pyroxene ± olivine (Rampone *et al.*, 1997); or (2) subsolidus crystallization of plagioclase (+ olivine) at the expense of spinel + pyroxene (Rampone *et al.*, 1993). In contrast to melt entrapment, percolative fractional crystallization and reactive porous flow involving interstitial crystallization of plagioclase + pyroxene segregates are expected to generate positive Eu anomalies in whole-rocks (Bodinier, 1988), whereas pyroxenes should be characterized by only minor or no negative Eu anomaly (Koga *et al.*, 2001). However, as discussed above, the scenario involving refertilization by melt entrapment can be ruled out for the studied samples because of their strong depletion in highly incompatible elements (Fig. 9). In agreement with textural evidence, this implies that plagioclase is of subsolidus origin in the Tolox pyroxenites.

Previous studies have shown that subsolidus re-equilibration of mantle rocks in the plagioclase stability field may greatly affect the REE composition of primary minerals (Rampone *et al.*, 1993). In Tolox, the effect of plagioclase crystallization on the REE composition of clinopyroxene is illustrated by the negative correlation between Eu_N/Eu^* and Yb_N (Fig. 12) showing that plagioclase crystallization causes not only Eu depletion but also HREE enrichment in clinopyroxene. This feature is consistent with plagioclase/clinopyroxene partition coefficients indicating that Eu is selectively partitioned into plagioclase—compared with other MREE—whereas HREE are more readily concentrated in clinopyroxene (McKay *et al.*, 1986). Similar to the HREE, the MREE are negatively correlated with Eu_N/Eu^* (not shown). However, the

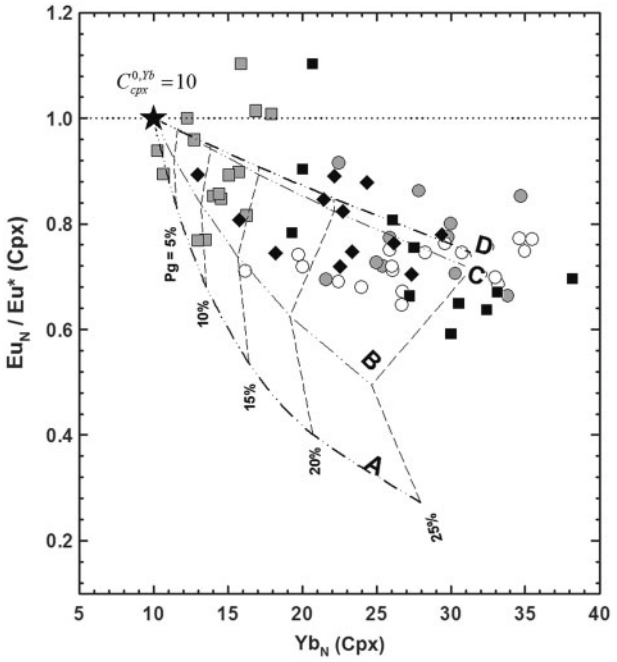

Fig. 12. Eu_N/Eu^* vs Yb_N [$Eu^* = 2 \times Eu_N/(Sm_N + Gd_N)$] for clinopyroxene analyzed by LA-ICP-MS for a lherzolite, two olivine websterites and two websterites from Tolox (symbols as in Fig. 10). The dot–dash curves show the effect of the formation of variable percentages of subsolidus plagioclase ('pg' labels, dashed lines) on the Eu_N/Eu^* and Yb_N of coexisting clinopyroxene. The curves are calculated using the mass-balance subsolidus reaction determined by Takazawa *et al.* (1996) and are shown for different available values of the clinopyroxene–plagioclase partition coefficient for Eu, Sm, Gd and Yb. Curve A: K_d values reported by Niu *et al.* (1996); curve B: K_d values reported by Bédard (1994); curve C: K_d values reported by Takazawa *et al.* (1996); curve *D*: K_d values from our study. The initial Eu_N/Eu^* and Yb_N values of clinopyroxene before subsolidus re-equilibration ($C^{0,Yb} = 10$; black star) was obtained by graphical extrapolation. N indicates chondrite normalized; normalizing values after Sun & McDonough (1989). (See text for further details.)

MREE/HREE ratios do not show the positive correlations with Eu_N/Eu^* that would be expected from plagioclase/clinopyroxene partitioning, indicating that 'primary' clinopyroxenes had variable MREE/HREE ratios before subsolidus re-equilibration.

As noted above, the clinopyroxenes devoid of a significant Eu negative anomaly (Eu/Eu^* in the range 0·9–1·1) are mostly found in websterites (notably in sample TOL-4a). However, the websterites also contain the clinopyroxenes showing the most pronounced negative Eu anomalies ($Eu/Eu^* < 0{\cdot}7$: sample TOL-5). The wider composition range of websterite clinopyroxene, compared with other rock types, reflects the highest proportion of both clinopyroxene and plagioclase in this facies. Primary clinopyroxene compositions are better preserved in the core of clinopyroxene aggregates, whereas the most re-equilibrated compositions are found where clinopyroxene is dispersed within plagioclase. In fact, all samples show a wide range of clinopyroxene compositions that may sometimes encompass the whole composition range of the Tolox section. Such small-scale inhomogeneities are more readily explained by subsolidus re-equilibration than by higher-temperature igneous processes.

To constrain further the effect of plagioclase crystallization on the REE composition of clinopyroxene, we calculated the redistribution of these elements between mineral phases resulting from the following plagioclase-forming reaction (Takazawa *et al.*, 1996):

$$0{\cdot}634\ \mathrm{Cpx} + 0{\cdot}291\ \mathrm{Opx} + 0{\cdot}075\ \mathrm{Sp} \rightarrow$$
$$0{\cdot}6\ \mathrm{Pg} + 0{\cdot}4\mathrm{Ol} \qquad (4)$$

where Sp stands for spinel and Pg for plagioclase. This reaction is applicable to lherzolite and silica-undersaturated pyroxenite compositions such as Ronda group C layers (Obata, 1980; Garrido & Bodinier, 1999). The concentration of a given trace element in clinopyroxene (C^r_{cpx}) after reaction (4) is given by

$$C^r_{cpx} = \frac{C^0_{cpx}(X^0_{cpx} + X^0_{opx}\cdot K^{opx/cpx} + X^0_{ol}\cdot K^{ol/cpx} + X^0_{sp}\cdot K^{sp/cpx})}{X^r_{cpx} + X^r_{opx}\cdot K^{opx/cpx} + X^r_{ol}\cdot K^{ol/cpx} + X^r_{pg}\cdot K^{pg/cpx}} \qquad (5)$$

where C^0_j and C^r_j represent the initial and final concentrations of a given trace element in mineral j (i.e. in the spinel- and plagioclase-peridotite facies, respectively), X^0_j and X^r_j the initial and final modal proportions of mineral j, with $\sum X^0_j = \sum X^r_j = 1$, and $K^{j/cpx}$ the partition coefficient of the trace element between phase j and clinopyroxene. Because of its low REE content, spinel is neglected in these calculations. The initial concentration of REE in clinopyroxene (C^0_{cpx}) can be evaluated from single analyses of clinopyroxene devoid of a Eu anomaly, or showing only subtle anomalies ($0{\cdot}9 \le Eu_N/Eu^* \le 1{\cdot}1$; Table 3; Fig. 10b). This approach yields an average Eu_N/Eu^* ratio of 0·98 and $Yb_N = 10$ in 'primary' clinopyroxene, consistent with a graphical extrapolation of clinopyroxene data at $Eu_N/Eu^* = 1$ on the Eu_N/Eu^* vs Yb_N diagram (Fig. 12).

The change in clinopyroxene composition as a result of subsolidus plagioclase crystallization was calculated with equation (5) for different sets of $K^{j/cpx}$ values. Experiments A and B were computed using $K^{j/cpx}$ values established by combining experimental mineral/melt partition coefficient values compiled by Niu *et al.* (1996) and Bédard (1994). For experiment C, we used $K^{j/cpx}$ values obtained by Takazawa *et al.* (1996) from ion probe analyses of minerals in subsolidus plagioclase lherzolites from the Horoman orogenic peridotite (Hokkaido, Japan). Experiment D was performed with $K^{j/cpx}$ values obtained from LA-ICP-MS analyses of mineral pairs in textural equilibrium in the Tolox samples. As an initial mode, we took that of an olivine–spinel websterite characterized by $X^0_{cpx} = 0{\cdot}35$, $X^0_{opx} = 0{\cdot}34$, $X^0_{ol} = 0{\cdot}22$ and $X^0_{sp} = 0{\cdot}09$.

Each numerical experiment was run up to the formation of 25 wt % plagioclase, which is the maximum amount of modal plagioclase observed in the Tolox pyroxenites. The results obtained with the different sets of partition coefficients are comparable in terms of Yb_N values. For $X^r_{pg} = 0{\cdot}25$, for instance, all experiments show an increase of C^r_{cpx} by a factor of 2·5–3·0 relative to C^0_{cpx}. However, the different results are variable with respect to Eu/Eu^*, depending mainly on the $K^{pg/cpx}_{Eu}$ values used in the experiments. The Tolox data are best fitted by experiments C and D, which yield Eu_N/Eu^* values around 0·75 in clinopyroxene at $X^r_{pg} = 0{\cdot}25$. These experiments use low $K^{pg/cpx}_{Eu}$ values (0·22 and 0·17, respectively). Experiments A and B use higher $K^{pg/cpx}_{Eu}$ values (1·32 and 0·67, respectively) and generate more pronounced negative Eu anomalies in clinopyroxene, with $Eu_N/Eu^* = 0{\cdot}3$–$0{\cdot}5$ at $X^r_{pg} = 0{\cdot}25$.

It is worth noting that low $K^{pg/cpx}_{Eu}$ values ($<0{\cdot}3$) are characteristic of natural plagioclase–clinopyroxene pairs equilibrated under subsolidus conditions. In addition to the Horoman and Tolox examples ($K^{pg/cpx}_{Eu} \sim 0{\cdot}2$), this is confirmed by the data reported by Rampone *et al.* (1993) for Ligurian plagioclase lherzolites ($K^{pg/cpx}_{Eu} \sim 0{\cdot}2$–$0{\cdot}3$). The $K^{pg/cpx}_{Eu}$ values obtained by combining experimental mineral/melt partition coefficients are variable, mostly in response to the variations of $K^{pg/melt}_{Eu}$ as a function of oxygen fugacity (Philpotts, 1970; Drake & Weill, 1975; Wilke & Behrens, 1999). However, the accepted values for igneous mantle processes are generally much higher that those recorded for subsolidus re-equilibration (e.g. 0·65–1·35; Bédard, 1994; Niu *et al.*, 1996). Interestingly, these values are confirmed by mineral compositions in gabbro veinlets in the Lanzo plagioclase lherzolite (Italian Alps). These veinlets record melt extraction or/and refertilization processes in shallow, MORB-type mantle (Boudier & Nicolas, 1977; Bodinier *et al.*, 1986, 1991; Piccardo *et al.*, 2007). The Piccardo *et al.* (2007) data yield $K^{pg/cpx}_{Eu}$ values in the range 0·7–1·5, comparable with experimental values.

The observed difference in $K^{pg/cpx}_{Eu}$ values suggests that the subsolidus spinel–plagioclase phase transition recorded by orogenic peridotites occurred in more oxidizing conditions than the igneous mantle processes recorded by the same massifs. This view is supported by the oxygen thermobarometry performed by Woodland *et al.* (1992) on the Ronda lherzolites, showing that the plagioclase-bearing samples are more oxidized than most of their plagioclase-free counterparts. The fO_2 variations recorded by single samples suggest progressive oxidation during the crystallization of plagioclase. However, on the basis of larger-scale fO_2 variations, Woodland *et al.* considered the mild oxidation attending the crystallization of plagioclase as inherited from some earlier event. They noted that the occurrence of amphibole also coincides with more oxidizing conditions and is independent of the presence of plagioclase. Based on this observation and on isotope geochemistry (Reisberg & Zindler, 1986–1987; Reisberg *et al.*, 1989, 1991), Woodland *et al.* (1992) ascribed the fO_2 variations in Ronda to the percolation of an oxidizing (and isotopically enriched) component (presumably a fluid phase) through a reduced (and isotopically depleted) peridotite protolith. In the light of recent works on the late, high-temperature evolution of the Ronda massif, it seems logical to relate this oxidizing component to the evolution of volatile-rich, small melt fractions that percolated at a late stage through the massif, shortly before its partial re-equilibration in the plagioclase peridotite facies. These melts are considered to be residual after melt-consuming reactions developed during the receding stages of the partial melting event recognized in Ronda (Van der Wal & Bodinier, 1996; Garrido & Bodinier, 1999; Garrido *et al.*, 2000; Lenoir *et al.*, 2001). These refertilization reactions occurred mostly in the granular domain—at the expense of which the plagioclase tectonites were developed—and might therefore explain the oxidized character of the plagioclase lherzolites. In this scheme, the possibility evoked by Woodland *et al.* (1992) that evolved fluids locally fluxed the plagioclase-forming reaction cannot be excluded.

On the same grounds, it is worth noting that the Horoman plagioclase lherzolites, which yield low $K^{pg/cpx}_{Eu}$ values similar to the Tolox samples (Takazawa *et al.*, 1996), were also possibly formed by igneous refertilization before their subsolidus re-equilibration in the plagioclase stability field (Saal *et al.*, 2001). Hence the relationships between oxygen fugacity and mantle refertilization probably deserves further investigation. In this frame, the distribution of Eu between plagioclase and clinopyroxene might prove to be useful as a tool to monitor reaction processes in orogenic peridotites, from partial melting to refertilization and subsolidus recrystallization.

Finally, a caveat raised by our results is that the re-equilibration of spinel peridotites and pyroxenites in the plagioclase stability field leads to substantial HREE enrichment in clinopyroxene. This enrichment largely exceeds in amplitude the negative Eu anomaly caused by plagioclase. Yb in cpx, for instance, is increased by a factor of three when Eu_N/Eu^* decreases by about 30% (Fig. 12). Using the REE composition of clinopyroxene to constrain melt–rock reactions therefore requires selecting undisturbed primary clinopyroxene compositions, devoid of significant Eu anomalies (Eu_N/Eu^* in the range 0·9–1·1; Table 3).

Numerical simulation of convex-upward REE patterns in clinopyroxene

The selected 'primary' clinopyroxenes are characterized by convex-upward normalized REE patterns and therefore plot in the lower-right quadrant of the (Ce/Nd) vs (Sm/Yb) diagram in Fig. 13. It is worth noting that some clinopyroxenes with significant negative Eu anomalies also show convex-upward REE patterns (Fig. 10) and have MREE/HREE ratios comparable with those of the

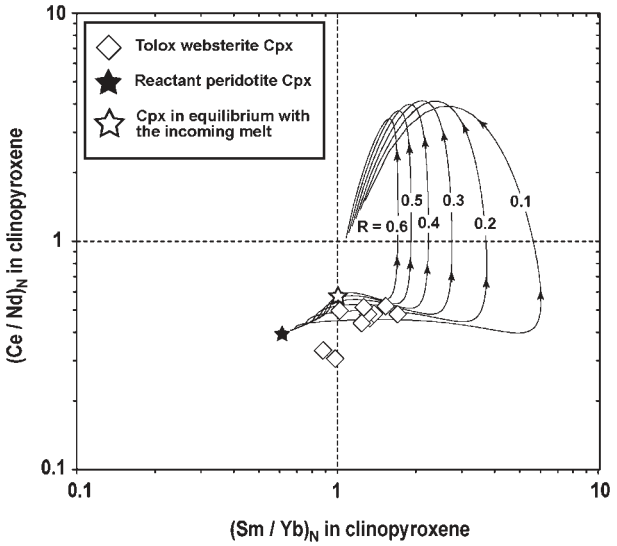

Fig. 13. Plot of $(Ce/Nd)_N$ vs $(Sm/Yb)_N$ in clinopyroxene showing the results of numerical modelling of REE ratio variations of clinopyroxene caused by reactive porous flow modelled with the 'Plate Model' of Vernières *et al.* (1997). N indicates chondrite normalized; normalizing values after Sun & McDonough (1989). The curves indicate the results of modelling for different R parameters (see text for further details). The arrows on the curves indicate the bottom-to-top cell evolution of melts in the reaction column. The composition of clinopyroxene for the reactant peridotites (open star) is the average composition of the clinopyroxene in the coarse granular peridotites of Lenoir *et al.* (2001). The composition of clinopyroxene in trace element exchange equilibrium with the incoming melts was calculated from the composition of aggregated melts produced by 15% incremental melting of the average composition of Ronda spinel tectonites reported by Lenoir *et al.* (2001) and Van der Wall & Bodinier (1996). ◇, Tolox pyroxenite–peridotite clinopyroxene devoid of Eu anomalies (see Fig. 10b).

selected, 'primary' clinopyroxenes, or even greater (e.g. $Sm_N/Yb_N = 0{\cdot}9$–$2{\cdot}0$ for the whole clinopyroxene dataset, compared with 0·9–1·7 for the 'primary' clinopyroxenes). However, as noted above, subsolidus re-equilibration with plagioclase increases HREE in clinopyroxene relative to MREE and therefore should decrease the Sm_N/Yb_N ratio in this mineral. Hence, one cannot exclude the possibility that the actual composition of the primary clinopyroxenes in the Tolox section was somewhat more variable than that recorded by the few, preserved clinopyroxenes that lack a negative Eu anomaly (Table 3). The whole range of primary clinopyroxenes probably included compositions characterized by even more convex normalized REE patterns than those selected on the basis of Eu fractionation.

This 'hump-shaped' REE distribution is considered as a proxy for the entire trace-element distribution in group C pyroxenites, marked by selective enrichment of moderately incompatible elements (notably Ti and MREE) relative to more incompatible and less incompatible elements. Cpx-rich crystal segregates and megacrysts crystallized from enriched (alkaline) mantle melts generally display convex-upward REE patterns (e.g. Irving, 1980; Irving & Frey, 1984; Bodinier *et al.*, 1987*b*). However, they are less depleted in LREE than the Tolox clinopyroxenes; they would plot in the upper part of the lower-right quadrant in Fig. 13, for $(Ce/Nd)_N$ values $\geq 0{\cdot}6$. Above all, alkaline crystal segregates do not show the strong depletion in highly incompatible elements relative to LREE that is typical of Ronda group C pyroxenites (Fig. 9). Melting of an enriched mantle component—plotting well inside the upper-right quadrant in Fig. 13—may theoretically generate convex REE patterns in residual clinopyroxene. However, as discussed above, the melting scenario is ruled out in Tolox by structural and mineralogical evidence. In contrast, the suggestion by Hellebrand *et al.* (2002) that 'hump-shaped' REE patterns can record refertilization by depleted melt is consistent with the structural and mineralogical arguments. We therefore evaluated this hypothesis with a simulation of melt-consuming, reactive porous flow aiming to reproduce the modal and REE compositions of Ronda group C layers.

We used for modelling the Plate Model of Vernières *et al.* (1997) in a configuration where infiltrated melts percolate through, and react with, a peridotite column composed of discrete 'reaction cells'. We took the average composition of the coarse granular subdomain as the initial composition for the peridotite column (open star in Fig. 13). This subdomain has a homogeneous, mildly refractory composition (cpx-poor lherzolite). It is considered to be residual after the passage of the melting front (Lenoir *et al.*, 2001) and to represent the protolith of the layered granular subdomain before refertilization (Van der Wal & Bodinier, 1996). As infiltrated melt, we took the composition of aggregated melts produced by 15% incremental melting of a mantle source with the average composition of the spinel-tectonite domain (closed star in Fig. 13). This region is considered as the lithospheric protolith of the Ronda massif before the passage of the melting front (Van der Wal & Bodinier, 1996; Lenoir *et al.*, 2001). Modelling was performed with a 100-cell column affected by the pyroxene-forming, melt-consuming reaction (1) previously used for Mg-number modelling. Several experiments were run with R values (mass ratio of precipitated pyroxenes to infiltrated melt) ranging from 0·1 to 0·6. All experiments show similar variation of the melt/rock ratio, marked by a rapid increase from $<0{\cdot}1$ in the upper cells to a 'plateau' at 1·30–1·35 in the lower half of the column (Fig. 14a). These values are within the range of the melt–rock ratios used for Mg-number modelling (0·0–1·5) (see Fig. 11). Similarly, the modal compositions vary from that of the protolith (70·6 wt % olivine, 21·4 wt % opx and 8·0 wt % cpx) atop the column to more fertile compositions, ranging from lherzolite for $R \leq 0{\cdot}1$ to olivine-free websterite for $R \geq 0{\cdot}6$, in the lower part of the column (Fig. 14b). REE contents in clinopyroxene show markedly different evolutions from HREE to LREE (Fig. 14c), as follows.

(1) HREE (Yb) are depleted in most parts of the column, relative to both clinopyroxene in equilibrium

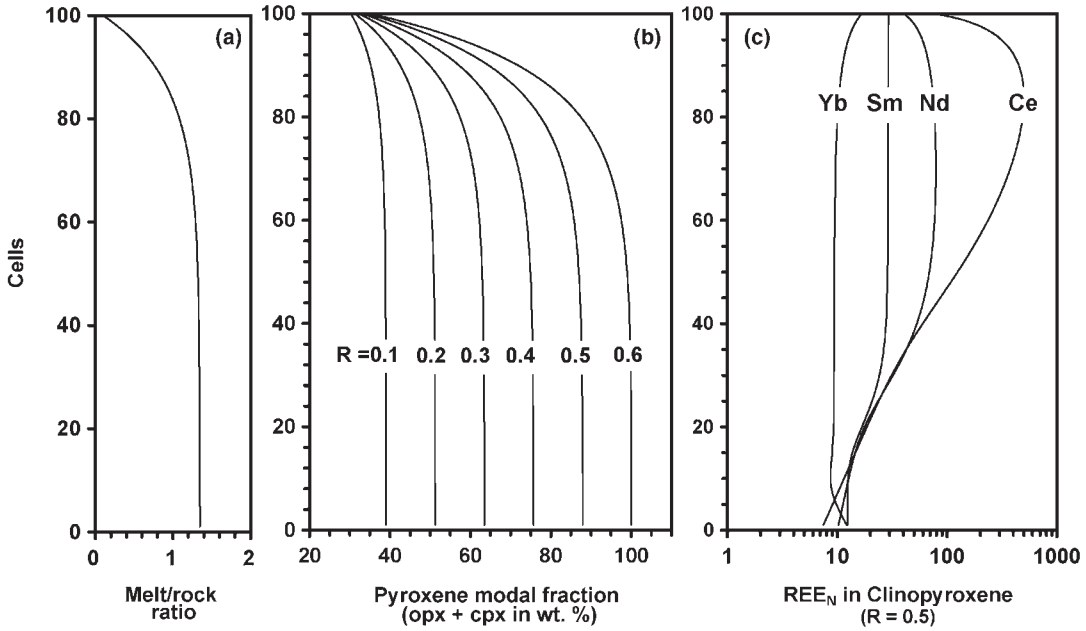

Fig. 14. Variation of the melt/rock ratio (Fig. 14a), the total modal content of pyroxene in wt % (Fig. 14b), and the content of selected REE_N in the equilibrium clinopyroxenes (Fig. 14c), from bottom to top cells of a reaction column of 100 cells obtained by modelling with the 'Plate Model' of Vernières *et al.* (1997) using the same input and reaction parameters as for the model shown in Fig. 13. (See text for further details.) N indicates chondrites normalized; normalizing values after Sun & McDonough (1989).

with the infiltrated melt, at the base of the column, and that in the initial peridotite, atop the column.

(2) MREE and LREE (Sm, Nd, Ce) are substantially (Sm) to strongly (Ce) enriched in the upper part of the column. Compared with clinopyroxene in equilibrium with the infiltrated melt, the enrichment factor increases with increasing incompatibility, from ~3 for Sm to ~50 for Ce. On the other hand, the enriched domain is increasingly restricted to the upper part of the column with increasing incompatibility of the elements. This feature illustrates the combination of chromatographic fractionation caused by melt transport and of the source effect of reaction in reactive porous flow systems (Godard *et al.*, 1995).

These REE variations result in curved trajectories in the $(Ce/Nd)_N$ vs $(Sm/Yb)_N$ diagram (Fig. 13). Based on $(Ce/Nd)_N$ values, two transient, enriched domains may be arbitrarily distinguished in the column, between the LREE-depleted composition of the initial peridotite and that of the infiltrated melt: (1) a lower domain characterized by convex-upward REE patterns and $(Ce/Nd)_N$ and $(Sm/Yb)_N$ values well inside the lower-right quadrant in Fig. 13; (2) an upper domain characterized by strongly LREE-enriched compositions and $(Ce/Nd)_N$ and $(Sm/Yb)_N$ values in the upper-right quadrant. The REE compositions obtained in lower part of the column match the compositions of most primary Tolox clinopyroxenes. Only two samples distinguished by $(Sm/Yb)_N$ close to unity and lower $(Ce/Nd)_N$ values would require a slightly more LREE-depleted infiltrated melt composition, compared with the other samples. In agreement with the constraints retrieved from Mg-number modelling, this lower part of the column is characterized by high melt/rock ratios (>1) and refertilized peridotite modes (lherzolite to websterite, depending on R values).

In contrast, the upper part of the column is characterized by lower melt–rock ratios (<1) and variable refertilization modes (Fig. 14a and b). This domain illustrates the segregation of residual, small melt fractions downstream of the main, melt-consuming reaction domain. This mechanism was advocated to explain strong enrichments in highly incompatible elements observed in 'cryptically' metasomatized mantle xenoliths (Bedini *et al.*, 1997; Ionov *et al.*, 2002), as well as in the wall-rocks of alkaline dykes within the Lherz peridotite, southern France (Bodinier *et al.*, 2004). In addition to highly incompatible elements, these melts are probably enriched in volatiles. Because of their low viscosity and solidification temperature, volatile-rich small volume melts may migrate through relatively cold mantle and infiltrate large volumes of lithospheric peridotites (McKenzie, 1989; Watson *et al.*, 1990). Such small melt fractions, residual after the refertilization reactions that generated the group C layers, probably migrated throughout the Ronda massif—including the preserved lithospheric spinel-tectonite domain (Van der Wal & Bodinier, 1996; Garrido *et al.*, 2000). Rarely, they crystallized in the

colder, outer part of the massif in the form of thin dykes of LREE-enriched Cr-diopside pyroxenites (Garrido & Bodinier, 1999). As noted above, the migration of these small melt fractions throughout the Ronda peridotite is a likely explanation for the fO_2 variations observed in the massif (Woodland *et al.*, 1992).

CONCLUSIONS AND GEODYNAMIC IMPLICATIONS

In the coarse-grained peridotite domain of the Ronda peridotite, Garrido & Bodinier (1999) recognized a group of Ti-rich layered pyroxenites (group C) characterized by swarms of parallel layers of spinel–plagioclase (± olivine) websterite and plagioclase lherzolite, intercalated with thin peridotite layers. Group C pyroxenites occur only in the Ronda layered coarse peridotite subdomain and the plagioclase-tectonite domain, which is located about 100 m beneath the recrystallization front. Our geochemical data and numerical modelling indicate that layered group C pyroxenites near the village of Tolox were formed by replacement of peridotites by melt-consuming reactions at pressure and temperature conditions close to the peridotite solidus.

The field characteristics and modal variations of the Ronda group C pyroxenites are reminiscent of those observed in gabbro sills at the Moho transition zone of the Oman ophiolite (Boudier & Nicolas, 1995; Korenaga & Kelemen, 1997) and other ophiolites (Marchesi *et al.*, 2006), which are interpreted as segregates crystallized at the thermal boundary layer represented by the oceanic Moho. Garrido & Bodinier (1999) suggested the formation of group C pyroxenites by refraction and channelling of upwelling partial melt atop a partial melting domain represented by the Ronda recrystallization front. Lenoir *et al.* (2001) have shown that the recrystallization front corresponded to a thermal boundary layer. Numerical models of oceanic spreading centres show that melt migration beneath a thermal boundary layer generates a high-porosity boundary layer as a result of dilation of the porous matrix near the solidus, where melt is being accumulated and/or frozen beneath the thermal boundary layer (Sparks & Parmentier, 1991; Spiegelman, 1993). Rabinowicz & Ceuleneer (2005) demonstrated that a decompaction channel located between the thermal boundary layer and the mantle upwelling may cause magma accumulation if there exists a dramatic drop in the amount of interstitial liquid in this channel. A similar scenario could be envisaged for the formation of the Ronda group C pyroxenites during rifting and thinning of subcontinental lithospheric mantle. Thermal erosion and melting of the subcontinental lithospheric mantle resulted in a thermal boundary layer beneath which melt accumulation occurred in a decompaction zone. The strong melt localization and high melt/rock ratios implied by the formation of the group C pyroxenites are accounted for by refraction and channelling of percolating melts below the freezing horizon represented by the recrystallization front constituting the base of the eroded subcontinental lithosphere. In this scheme, the group C layers would trace the position of the solidus isotherm receding down to gradually deeper mantle levels upon thermal relaxation and cooling. Although strongly heterogeneous on a centimeter to tens of meter scale, the Ronda 'layered granular' subdomain and the 'plagioclase-tectonite' domains are, on average, significantly more fertile than the residual 'coarse granular' subdomain. These compositional differences suggest that such a process induced refertilization of the melted lithosphere.

Finally, plagioclase in Tolox samples is of subsolidus origin, demonstrating that melt–rock reaction processes involved in the fertilization of Tolox peridotites occurred in the spinel facies under P–T conditions roughly similar to those recorded for the development of the Ronda recrystallization melting front (Garrido & Bodinier, 1999; Lenoir *et al.*, 2001). In Alpine orogenic peridotites, formation of plagioclase peridotites has been ascribed either to subsolidus re-equilibration of spinel peridotites or to igneous fertilization by basaltic melts of peridotites in the plagioclase lherzolite facies (Pognante *et al.*, 1985; Bodinier, 1988; Rampone *et al.*, 1993, 1995, 1996, 1997; Bodinier & Godard, 2003; Piccardo *et al.*, 2007). In Ronda, as in abyssal peridotites, igneous fertilization in the plagioclase lherzolite facies ($<1{\cdot}0$ GPa) would imply melt–peridotite reactions involving igneous plagioclase in a thermally eroded and extremely thinned lithosphere (<33 km). Alternatively, melt–rock reactions in Ronda occurred mostly in the spinel facies and therefore in a thicker, though thinned, continental lithosphere (1·5 GPa, ~50 km; Garrido & Bodinier, 1999; Lenoir *et al.*, 2001). These spinel-facies rocks were subsequently equilibrated at subsolidus P–T conditions in the plagioclase lherzolite field as originally proposed by Obata (1980).

ACKNOWLEDGEMENTS

We are indebted to Simone Pourtales for assistance during ICP-MS analyses at ISTEEM. We acknowledge Dr Michel Grégoire, Dr Elisabetta Rampone and an anonymous reviewer for their constructive reviews. This work has been supported by the Spanish 'Ministerio de Educación y Ciencia' through a 'Ramón y Cajal' fellowship to C. J. Garrido, 'Acción Integrada Hispano-Francesa HF2005-0066' and research grants CGL2004-00622, BTE2006-1489 and PCI2006-A9-0580, and by the 'Junta de Andalucía' research group RNM-0131.

REFERENCES

Allègre, C. J. & Turcotte, D. L. (1986). Implications of a two-component marble-cake mantle. *Nature* **263**, 123–127.

Becker, H. (1996). Geochemistry of garnet peridotite massifs from lower Austria and the composition of deep lithosphere beneath a Palaeozoic convergent plate margin. *Chemical Geology* **134**, 49–65.

Becker, H., Carlson, R. W. & Shirey, S. B. (2004). Slab-derived osmium and isotopic disequilibrium in garnet pyroxenites from a Paleozoic convergent plate margin (lower Austria). *Chemical Geology* **208**, 141–156.

Bédard, J. H. (1994). A procedure for calculating the equilibrium distribution of trace-elements among the minerals of cumulate rocks, and the concentration of trace-elements in the coexisting liquids. *Chemical Geology* **118**, 143–153.

Bedini, R. M., Bodinier, J. L., Dautria, J. M. & Morten, L. (1997). Evolution of LILE-enriched small melt fractions in the lithospheric mantle: a case study from the East African Rift. *Earth and Planetary Science Letters* **153**, 67–83.

Bedini, R. M., Bodinier, J.-L. & Vernières, J. (2002). Numerical simulation of Mg–Fe partitioning during melting and melt–rock reaction in the shallow upper mantle. *Extended Abstracts, Proceedings of 4th International Orogenic Lherzolites and Mantle Processes Conference*. Japan: Samani (unpublished).

Blichert-Toft, J., Albarède, F. & Kornprobst, J. (1999). Lu–Hf isotope systematics of garnet pyroxenites from Beni Bousera, Morocco: Implications for basalt origin. *Science* **283**, 1303–1306.

Bodinier, J.-L. (1988). Geochemistry and petrogenesis of the Lanzo peridotite body, western Alps. *Tectonophysics* **149**, 67–88.

Bodinier, J. L. & Godard, M. (2003). Orogenic, ophiolitic, and abyssal peridotites. In: Carlson, R. W. (ed.) *Treatise on Geochemistry. 2. Geochemistry of the Mantle and Core*. Amsterdam: Elsevier, pp. 103–170.

Bodinier, J. L., Guiraud, M., Dupuy, C. & Dostal, J. (1986). Geochemistry of basic dikes in the Lanzo massif (Western Alps)—petrogenetic and geodynamic implications. *Tectonophysics* **128**, 77–95.

Bodinier, J.-L., Guiraud, M., Fabries, J., Dostal, J. & Dupuy, C. (1987*a*). Petrogenesis of layered pyroxenites from the Lherz, Freychinède and Prades ultramafic bodies (Ariège, French Pyrenées). *Geochimica et Cosmochimica Acta* **51**, 279–290.

Bodinier, J. L., Fabries, J., Lorand, J. P., Dostal, J. & Dupuy, C. (1987*b*). Geochemistry of amphibole pyroxenite veins from the Lherz and Freychinède ultramafic bodies (Ariège, French Pyrenées). *Bulletin de Minéralogie* **110**, 345–358.

Bodinier, J.-L., Menzies, M. A. & Thirlwall, M. (1991). Continental to oceanic mantle transition—REE and Sr–Nd isotopic geochemistry of the Lanzo lherzolite massif. *Journal of Petrology*, Special issue 'Orogenic Lherzolites and Mantle Processes', 191–210.

Bodinier, J. L., Menzies, M. A., Shimizu, N., Frey, F. A. & McPherson, E. (2004). Silicate, hydrous and carbonate metasomatism at Lherz, France: Contemporaneous derivatives of silicate melt–harzburgite reaction. *Journal of Petrology* **45**, 299–320.

Booth-Rea, G., Azañon, J. M., Martínez-Martínez, J. M., Vidal, O. & García Dueñas, V. (2005). Contrasting structural and *P–T* evolution of tectonic units in the southeastern Betics: Key for understanding the exhumation of the Alboran Domain HP/LT crustal rocks (western Mediterranean). *Tectonics* **24**, doi:10.1029/2004TC001640.

Boudier, F. & Nicolas, A. (1977). Structural controls on partial melting in the Lanzo peridotite. In: Dick, H. J. B. (ed.) *Magma Genesis*. Portland: State of Oregon Department of Geology and Mining Industries, pp. 63–79.

Boudier, F. & Nicolas, A. (1995). Nature of the Moho Transition Zone in the Oman Ophiolite. *Journal of Petrology* **36**, 777–796.

Davies, G. R., Nixon, P. H., Pearson, D. G. & Obata, M. (1993). Tectonic implications of graphitized diamonds from the Ronda Peridotite massif, Southern Spain. *Geology* **21**, 471–474.

Drake, M. J. & Weill, D. F. (1975). Partition of Sr, Ba, Ca, Y, Eu^{2+}, Eu^{3+}, and other REE between plagioclase feldspar and magmatic liquid—Experimental study. *Geochimica et Cosmochimica Acta* **39**, 689–712.

Frey, F. A., Suen, C. J. & Stockman, H. W. (1985). The Ronda high-temperature peridotite—geochemistry and petrogenesis. *Geochimica et Cosmochimica Acta* **49**, 2469–2491.

Garrido, C. J. & Bodinier, J. L. (1999). Diversity of mafic rocks in the Ronda peridotite: Evidence for pervasive melt–rock reaction during heating of subcontinental lithosphere by upwelling asthenosphere. *Journal of Petrology* **40**, 729–754.

Garrido, C. J., Bodinier, J. L. & Alard, O. (2000). Incompatible trace element partitioning and residence in anhydrous spinel peridotites and websterites from the Ronda orogenic peridotite. *Earth and Planetary Science Letters* **181**, 341–358.

Gervilla, F. & Remaïdi, M. (1993). Field trip to the Ronda ultramafic massif: an example of asthenosphere–lithosphere interaction? *Ofioliti* **18**, 21–35.

Godard, M., Bodinier, J. L. & Vasseur, G. (1995). Effects of mineralogical reactions on trace-element redistributions in mantle rocks during percolation processes—a chromatographic approach. *Earth and Planetary Science Letters* **133**, 449–461.

Hamelin, B. & Allègre, C. J. (1988). Lead isotope study of orogenic lherzolite massifs. *Earth and Planetary Science Letters* **91**, 117–131.

Hanson, G. N. & Langmuir, C. H. (1978). Modeling of major elements in mantle–melt systems using trace-element approaches. *Geochimica et Cosmochimica Acta* **42**, 725–741.

Harte, B., Hunter, R. H. & Kinny, P. D. (1993). Melt geometry, movement and crystallization, in relation to mantle dykes, veins and metasomatism. *Philosophical Transactions of the Royal Society of London, Series A* **342**, 1–21.

Hauri, E. H. (1996). Major element variability in the Hawaiian mantle plume. *Nature* **382**, 415–419.

Hellebrand, E., Snow, J. E., Hoppe, P. & Hofmann, A. W. (2002). Garnet-field melting and late-stage refertilization in 'residual' abyssal peridotites from the Central Indian Ridge. *Journal of Petrology* **43**, 2305–2338.

Herzberg, C. (2006). Petrology and thermal structure of the Hawaiian plume from Mauna Kea volcano. *Nature* **444**, 605–609.

Hirschmann, M. M. & Stolper, E. M. (1996). A possible role for garnet pyroxenite in the origin of the 'garnet signature' in MORB. *Contributions to Mineralogy and Petrology* **124**, 185–208.

Hofmann, A. W. & White, W. M. (1982). Mantle plumes from ancient oceanic-crust. *Earth and Planetary Science Letters* **57**, 421–436.

Ionov, D. A., Savoyant, L. & Dupuy, C. (1992). Application of the ICP-MS technique to trace-element analysis of peridotites and their minerals. *Geostandards Newsletter* **16**, 311–315.

Ionov, D. A., Bodinier, J. L., Mukasa, S. B. & Zanetti, A. (2002). Mechanisms and sources of mantle metasomatism: Major and trace element compositions of peridotite xenoliths from Spitsbergen in the context of numerical modelling. *Journal of Petrology* **43**, 2219–2259.

Ionov, D. A., Chanefo, I. & Bodinier, J. L. (2005). Origin of Fe-rich lherzolites and wehrlites from Tok, SE Siberia by reactive melt percolation in refractory mantle peridotites. *Contributions to Mineralogy and Petrology* **150**, 335–353.

Irving, A. J. (1980). Petrology and geochemistry of composite ultramafic xenoliths in alkaline basalts and implications for magmatic processes within the mantle. *American Journal of Science* **280-A**, 389–426.

Irving, A. J. & Frey, F. A. (1984). Trace-element abundances in megacrysts and their host basalts—constraints on partition-coefficients and megacryst genesis. *Geochimica et Cosmochimica Acta* **48**, 1201–1221.

Jochum, K. P., Seufert, H. M. & Thirwall, M. F. (1990). Muti-element analysis of 15 international standard rocks by isotope-dilution

spark source mass spectrometry (ID-SSMS). *Analytical Chemistry* **331**, 104–110.

Kelemen, P. B., Dick, H. J. B. & Quick, J. E. (1992). Formation of harzburgite by pervasive melt rock reaction in the upper mantle. *Nature* **358**, 635–641.

Koga, K. T., Kelemen, P. B. & Shimizu, N. (2001). Petrogenesis of the crust–mantle transition zone and the origin of lower crustal wehrlite in the Oman ophiolite. *Geochemistry, Geophysics, Geosystems* 2, paper number 2000GC000132.

Korenaga, J. & Kelemen, P. B. (1997). Origin of gabbro sills in the Moho transition zone of the Oman ophiolite: Implications for magma transport in the oceanic lower crust. *Journal of Geophysical Research—Solid Earth* **102**, 27729–27749.

Kornprobst, J., Piboule, M., Roden, M. & Tabit, A. (1990). Corundum-bearing garnet clinopyroxenites at Beni-Bousera (Morocco)—original plagioclase-rich gabbros recrystallized at depth within the mantle. *Journal of Petrology* **31**, 717–745.

Lenoir, X., Garrido, C. J., Bodinier, J. L., Dautria, J. M. & Gervilla, F. (2001). The recrystallization front of the Ronda peridotite: Evidence for melting and thermal erosion of subcontinental lithospheric mantle beneath the Alboran basin. *Journal of Petrology* **42**, 141–158.

Loubet, M. & Allègre, C. J. (1982). Trace elements in orogenic lherzolites reveal the complex history of the upper mantle. *Nature* **298**, 809–814.

Maaløe, S. & Scheie, A. (1982). The permeability controlled accumulation of primary magma. *Contributions to Mineralogy and Petrology* **81**, 350–357.

Marchesi, C., Garrido, C. J., Godard, M., Proenza, J. A., Gervilla, F. & Blanco-Moreno, J. (2006). Petrogenesis of highly depleted peridotites and gabbroic rocks from the Mayari–Baracoa Ophiolitic Belt (eastern Cuba). *Contributions to Mineralogy and Petrology* **151**, 717–736, doi: 710.1007/s00410-00006-00089-00410.

McKay, G. A., Wagstaff, J. & Yang, S.-R. (1986). Clinopyroxene REE distribution coefficients for shergottites: The REE content of the Shergotty melt. *Geochimica et Cosmochimica Acta* **50**, 927–937.

McKenzie, D. (1984). The generation and compaction of partially molten rock. *Journal of Petrology* **25**, 713–765.

McKenzie, D. (1989). Some remarks on the movement of small melt fractions in the Mantle. *Earth and Planetary Science Letters* **95**, 53–72.

Morishita, T. & Arai, S. (2001). Petrogenesis of corundum-bearing mafic rock in the Horoman peridotite complex, Japan. *Journal of Petrology* **42**, 1279–1299.

Morishita, T., Arai, S. & Gervilla, F. (2001). High-pressure aluminous mafic rocks from the Ronda peridotite massif, southern Spain: significance of sapphirine- and corundum-bearing mineral assemblages. *Lithos* **57**, 143–161.

Niu, Y. L., Waggoner, D. G., Sinton, J. M. & Mahoney, J. J. (1996). Mantle source heterogeneity and melting processes beneath seafloor spreading centers: The East Pacific Rise, 18°–19°S. *Journal of Geophysical Research—Solid Earth* **101**, 27711–27733.

Obata, M. (1980). The Ronda peridotite—garnet-lherzolite, spinel-lherzolite, and plagioclase-lherzolite facies and the *P–T* trajectories of a high-temperature mantle intrusion. *Journal of Petrology* **21**, 533–572.

Obata, M. & Nagahara, N. (1987). Layering of alpine-type peridotite and the segregation of partial melt in the upper mantle. *Journal of Geophysical Research* **92**, 3467–3474.

Palme, H. & Jones, A. (2003). Solar System abundances of the elements. In: Carlson, R. W. (ed.) *Treatise on Geochemistry. 2. Geochemistry of the Mantle and Core*. Amsterdam: Elsevier, pp. 41–61.

Pearson, D. G. & Nowell, G. M. (2004). Re–Os and Lu–Hf isotope constraints on the origin and age of pyroxenites from the Beni Bousera peridotite massif; implications for mixed peridotite–pyroxenite mantle sources. *Journal of Petrology* **45**, 439–455.

Pearson, D. G., Davies, G. R., Nixon, P. H. & Milledge, H. J. (1989). Graphitized diamonds from a peridotite massif in Morocco and implications for anomalous diamond ocurrences. *Nature* **338**, 60–62.

Pearson, D. G., Davies, G. R. & Nixon, P. H. (1993). Geochemical constraints on the petrogenesis of diamond facies pyroxenites from the Beni Bousera peridotite massif, North Morocco. *Journal of Petrology* **34**, 125–172.

Philpotts, J. A. (1970). Redox estimation from a calculation of Eu^{2+} and Eu^{3+} concentrations in natural phases. *Earth and Planetary Science Letters* **9**, 257.

Piccardo, G. B., Zanetti, A. & Müntener, O. (2007). Melt/peridotite interaction in the Southern Lanzo peridotite: field, textural and geochemical evidence. *Lithos* **94**, 181–209.

Platt, J. P., Argles, T. W., Carter, A., Kelley, S. P., Whitehouse, M. J. & Lonergan, L. (2003). Exhumation of the Ronda peridotite and its crustal envelope: constraints from thermal modelling of a *P–T*–time array. *Journal of the Geological Society, London* **160**, 655–676.

Pognante, U., Rosli, U. & Toscani, L. (1985). Petrology of ultramafic and mafic rocks from the Lanzo peridotite body (Western Alps). *Lithos* **18**, 201–214.

Polvé, M. & Allègre, C. J. (1980). Orogenic lherzolite complexes studied by ^{87}Rb–^{87}Sr: a clue to understand the mantle convection processes?. *Earth and Planetary Science Letters* **51**, 71–93.

Precigout, J., Gueydan, F., Gapais, D., Garrido, C. J. & Essaifi, A. (2007). Strain localisation in the subcontinental mantle—a ductile alternative to the brittle mantle. *Tectonophysics* **445**, 318–336.

Prinzhofer, A., Lewin, E. & Allègre, C. J. (1989). Stochastic melting of the marble cake mantle: evidence from local study of the East Pacific Ridge at 12°50′. *Earth and Planetary Science Letters* **92**, 189–206.

Rabinowicz, M. & Ceuleneer, G. (2005). The effect of sloped isotherms on melt migration in the shallow mantle: a physical and numerical model based on observations in the Oman ophiolite. *Earth and Planetary Science Letters* **3–4**, 231–246.

Rampone, E., Piccardo, G. B., Vannucci, R., Bottazzi, P. & Ottolini, L. (1993). Subsolidus reactions monitored by trace-element partitioning—the spinel-facies to plagioclase-facies transition in mantle peridotites. *Contributions to Mineralogy and Petrology* **115**, 1–17.

Rampone, E., Hofmann, A. W., Piccardo, G. B., Vannucci, R., Bottazzi, P. & Ottolini, L. (1995). Petrology, mineral and isotope geochemistry of the External Liguride Peridotites (Northern Apennines, Italy). *Journal of Petrology* **36**, 81–105.

Rampone, E., Hofmann, A. W., Piccardo, G. B., Vannucci, R., Bottazzi, P. & Ottolini, L. (1996). Trace element and isotope geochemistry of depleted peridotites from an N-MORB type ophiolite (Internal Liguride, N Italy). *Contributions to Mineralogy and Petrology* **123**, 61–76.

Rampone, E., Piccardo, G. B., Vannucci, R. & Bottazzi, P. (1997). Chemistry and origin of trapped melts in ophiolitic peridotites. *Geochimica et Cosmochimica Acta* **61**, 4557–4569.

Reisberg, L. & Lorand, J. P. (1995). Longevity of sub-continental mantle lithosphere from osmium isotope systematics in orogenic peridotite massifs. *Nature* **376**, 159–162.

Reisberg, L. & Zindler, A. (1986–1987). Extreme isotopic variations in the upper mantle: evidence from Ronda. *Earth and Planetary Sciences Letters* **81**, 29–45.

Reisberg, L. C., Zindler, A. & Jagoutz, E. (1989). Futher Sr and Nd isotopic results from peridotites of the Ronda Ultramafic Complex. *Earth and Planetary Science Letters* **96**, 161–180.

Reisberg, L. C., Allègre, C. J. & Luck, J. M. (1991). The Re–Os systematics of the Ronda Ultramafic Complex of southern Spain. *Earth and Planetary Science Letters* **105**, 196–213.

Remaïdi, M. (1993). Étude pétrologique et géochimique d'une association péridotites refractaires–pyroxenites dans le Massif de Ronda (Espagne). Ph.D. Thesis, Université de Montpellier II, 437 pp.

Saal, A. E., Takazawa, E., Frey, F. A., Shimizu, N. & Hart, S. R. (2001). Re–Os isotopes in the Horoman peridotite: evidence for refertilization? *Journal of Petrology* **42**, 25–37.

Salters, V. J. M. & Dick, H. J. B. (2002). Mineralogy of the mid-ocean-ridge basalt source from neodymium isotopic composition of abyssal peridotites. *Nature* **418**, 68–72.

Sanchez-Rodriguez, L. & Gebauer, D. (2000). Mesozoic formation of pyroxenites and gabbros in the Ronda area (southern Spain), followed by Early Miocene subduction metamorphism and emplacement into the middle crust: U–Pb sensitive high-resolution ion microprobe dating of zircon. *Tectonophysics* **316**, 19–44.

Sharma, M., Wasserburg, G. J., Papanastassiou, D. A., Quick, J. E., Sharkov, E. V. & Laz'ko, E. E. (1995). High $^{143}Nd/^{144}Nd$ in extremely depleted mantle rocks. *Earth and Planetary Science Letters* **135**, 101–114.

Shervais, J. W. (1979). Thermal emplacement model for the Alpine lherzolite massif at Balmuccia, Italy. *Journal of Petrology* **20**, 795–820.

Sobolev, A. V., Hofmann, A. W., Sobolev, S. V. & Nikogosian, I. K. (2005). An olivine-free mantle source of Hawaiian shield basalts. *Nature* **434**, 590–597.

Sparks, D. W. & Parmentier, E. M. (1991). Melt extraction from the mantle beneath spreading centers. *Earth and Planetary Science Letters* **105**, 368–377.

Spiegelman, M. (1993). Physics of melt extraction—theory, implications and applications. *Philosophical Transactions of the Royal Society of London. Series A* **342**, 23–41.

Suen, C. J. & Frey, F. A. (1987). Origins of the mafic and ultramafic rocks in the Ronda Peridotite. *Earth and Planetary Science Letters* **85**, 183–202.

Sun, S.-S. & McDonough, W. F. (1989). Chemical and isotopic systematics of oceanic basalts: implications for mantle composition and processes. In: Saunders, A. D. & Norry, M. J. (eds) *Magmatism in the Ocean Basins. Geological Society, London, Special Publications* **42**, 313–345.

Takazawa, E., Frey, F. A., Shimizu, N. & Obata, M. (1996). Evolution of the Horoman Peridotite (Hokkaido, Japan); implications from pyroxene compositions. *Chemical Geology* **134**, 3–26.

Tarantola, A. & Valette, B. (1982). Generalized non-linear inverse problems solved using least-squares criterion. *Reviews of Geophysics and Space Physics* **20**, 219–232.

Ulmer, P. (1989). The dependence of Fe^{2+}–Mg cation-partitioning between olivine and basaltic liquid on pressure, temperature and composition: an experimental study to 30 kbars. *Contributions to Mineralogy and Petrology* **101**, 261–273.

Van der Wal, D. & Bodinier, J. L. (1996). Origin of the recrystallisation front in the Ronda peridotite by km-scale pervasive porous melt flow. *Contributions to Mineralogy and Petrology* **122**, 387–405.

Van der Wal, D. & Vissers, R. L. M. (1993). Uplift and emplacement of upper-mantle rocks in the Western Mediterranean. *Geology* **21**, 1119–1122.

Van der Wal, D. & Vissers, R. L. M. (1996). Structural petrology of the Ronda peridotite, SW Spain: Deformation history. *Journal of Petrology* **37**, 23–43.

Vauchez, A. & Garrido, C. J. (2001). Seismic properties of an asthenospherized lithospheric mantle: constraints from lattice preferred orientations in peridotite from the Ronda massif. *Earth and Planetary Science Letters* **192**, 235–249.

Vernières, J., Godard, M. & Bodinier, J. L. (1997). A plate model for the simulation of trace element fractionation during partial melting and magma transport in the Earth's upper mantle. *Journal of Geophysical Research—Solid Earth* **102**, 24771–24784.

Watson, B. E., Brenan, J. M. & Baker, D. R. (1990). Distribution of fluids in the continental mantle. In: Menzies, M. A. (ed.) *Continental Mantle*. Oxford: Clarendon Press, pp. 111–125.

Wilke, M. & Behrens, H. (1999). The dependence of the partitioning of iron and europium between plagioclase and hydrous tonalitic melt on oxygen fugacity. *Contributions to Mineralogy and Petrology* **137**, 102–114.

Wilshire, H. G., Nielson, J. E., Pike, J. E. N., Meyer, C. E. & Schwarzman, E. C. (1980). Amphibole-rich veins in lherzolite xenoliths, Dish Hill and Deadman Lake, California. *American Journal of Science* **280A**, 576–593.

Woodland, A. B., Kornprobst, J. & Wood, B. J. (1992). Oxygen thermobarometry of orogenic lherzolite massifs. *Journal of Petrology* **33**, 203–230.